
Chapter 16

Ground Echo

Richard K. Moore

The University of Kansas

16.1 INTRODUCTION

Radar ground return is described by σ^0 , the differential scattering cross section, or scattering coefficient (scattering cross section per unit area), rather than by the total scattering cross section σ used for discrete targets.¹ Since the total cross section σ of a patch of ground varies with the illuminated area that is determined by the geometric radar parameters (pulse width, beamwidth, etc.), σ^0 was introduced to obtain a coefficient independent of these parameters.

Use of a differential scattering cross section implies that the return from the ground is contributed by a large number of scattering elements whose phases are independent. This is primarily because of differences in distance that, although small fractions of total distance, are many wavelengths. Superposition of power is possible for the computation of average returns. If this condition is not applicable to a particular ground target, the differential-scattering cross-section concept has no meaning for that target. For example, a very fine-resolution radar might be able to resolve a part of a car; the smooth surfaces on the car would not be properly represented by σ^0 . On the other hand, a coarser radar might look at many cars in a large parking lot, and a valid σ^0 for the parking lot could be determined.

If a region illuminated at one time by a radar contains n scattering elements and the above criterion is satisfied so that power may be added, the radar equation for average power becomes

$$\bar{P}_r = \sum_i^n \frac{P_{ti} G_{ti} A_{ri} \sigma_i}{(4\pi R_i^2)^2} = \sum_i^n \frac{P_{ti} G_{ti} A_{ri} (\sigma_i / \Delta A_i) \Delta A_i}{(4\pi R_i^2)^2}$$

Here, ΔA_i is an element of surface area; and P_{ti} (power transmitted toward point i), G_{ti} (gain in direction of point i), and A_{ri} (receiving equivalent aperture in direction of point i) are values of P_t , G_t , and A_r appropriate for an element at the location of ΔA_i . The factor in parentheses in the numerator of the right-hand expression is the incremental scattering cross section for element i , but this concept is meaningful only in an average. Thus, the average power returned is given by

$$\bar{P}_r = \sum_i^n \frac{P_{ti} G_{ti} A_{ri} \sigma^0 \Delta A_i}{(4\pi R_i^2)^2}$$

Here, σ^0 has been used to denote the average value of $\sigma_i/\Delta A_i$. In this formulation, we may pass in the limit from the finite sum to the integral given by

$$\bar{P}_r = \frac{1}{(4\pi)^2} \int_{\text{Illuminated area}} \frac{P_t G_t A_r \sigma^0 dA}{R^4} \quad (16.1)$$

This integral is not really correct, for there is a minimum size for real, independent scattering centers. Nevertheless, the concept is widely used and is applicable as long as the illuminated area is large enough to contain many such centers.

Figure 16.1 illustrates the geometry associated with Eq. 16.1. Note that for a rectangular pulse, P_t is either zero or the peak transmitter power; but for other pulse shapes, the variation with t (or R) is significant. Actual pulses are often approximated by rectangular pulses with widths equal to their half-power widths. Real pulses cannot be rectangular after passing through real transmitter, antenna, and receiver bandwidths. The transmitting-antenna gain and receiving-antenna aperture are functions of the elevation and azimuth angles:

$$G_t = G_t(\theta, \phi) \quad A_r = A_r(\theta, \phi) \quad (16.2a)$$

The differential scattering cross section itself is a function of both *look angle* (θ, ϕ) and ground location:

$$\sigma^0 = \sigma^0(\theta, \phi, \text{location}) \quad (16.2b)$$

The integral of Eq. 16.1 must be inverted when σ^0 is measured. With narrow beams and short pulses, the inversion is relatively easy, but with the wider beams and longer pulses used in many measurements, the values obtained are sometimes poorly defined.

Some authors² use a scattering cross section per unit projected area rather than per unit ground area. Figure 16.2 illustrates by using a *side view* the difference

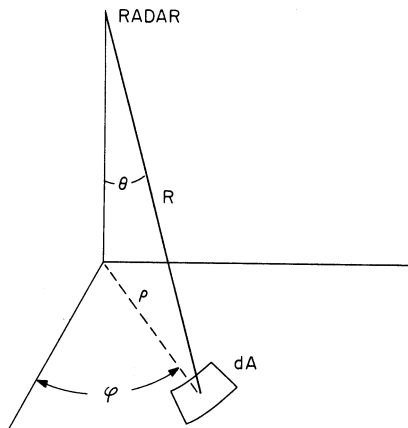


FIGURE 16.1 Geometry of the radar equation

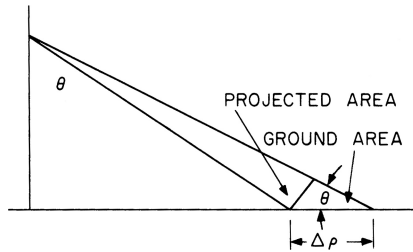


FIGURE 16.2 Ground area and projected area

between ground area and projected area. The ground area is proportional to $\Delta\rho$, and the projected area is smaller. Thus,

$$\sigma^0 A = \gamma d(\text{projected area}) = \gamma \cos \theta dA \quad (16.3)$$

or

$$\sigma^0 = \gamma \cos \theta$$

Since both γ and σ^0 are called scattering coefficients, readers of the literature must be especially careful to determine which is being used by a particular author.

Radar astronomers use a different σ^3 :

$$\frac{\text{total return power from entire surface}}{\text{power returned from perfect isotropic sphere of same radius}} \quad (16.4)$$

The resulting value for σ is usually much smaller than σ^0 for the planet at vertical incidence and is larger than the values of σ^0 near grazing incidence (return from the limb of the planet).

Relative Importance of Theory and Empiricism. The theory of radar ground return has been the subject of many publications.^{4,5} The various theories, insofar as they can be confirmed by experiment, provide bases for judging the effects of variations in the dielectric properties of the ground, of the roughness of the ground and nature of vegetative or snow cover, of radar wavelength, and of angle of incidence. Viewed as aids to insight, radar ground-return theories can be extremely useful.

The validity of any ground-return theory must depend on the mathematical model used to describe the surface, as well as on the approximations required to obtain answers. Even the simplest ground surface, the sea, is extremely difficult to describe accurately; it is homogeneous to beyond the skin depth, contains relatively modest slopes, and (except for spray) has no part above another part of the surface. At grazing angles, shadowing of one wave by another might occur. Land surfaces are much more difficult to describe: Imagine an adequate mathematical description of the shape of a forest (when every leaf and pine needle must be described). Furthermore, land surfaces are seldom homogeneous either horizontally or with depth.

Since a true mathematical description of the ground surface appears out of the question, empirical measurements are necessary to describe the radar return from natural surfaces. The role of theory is to aid in interpreting these measurements and to suggest how they may be extrapolated.

Available Scattering Information. Prior to 1972, the lack of coordinated research programs over the necessary long period resulted in only one really usable set of measurements, developed at Ohio State University.^{2,6} Since that time, extensive measurements have been made from trucks and helicopters by the University of Kansas,^{8,9} groups in the Netherlands,^{10,11} and several groups in France.^{12,13,14} These measurements concentrated especially on vegetation, with the Kansas measurements also including some work on snow and extensive work on sea ice. Most of these measurements were in the 10° to 80° range of incidence angles. Measurements near vertical are scarcer.^{15,16} Well-controlled experiments near grazing are also scarce except for a major Lincoln Laboratory program.¹⁷

Airborne measurements are necessary to make larger scattering areas accessible. Although airborne programs for special purposes have been legion, curves of scattering coefficient versus angle for a known homogeneous area are scarce. The work at the MIT Radiation Laboratory¹⁸ was early. Work by Philco Corporation,¹⁹ Goodyear Aerospace Corporation,²⁰ General Precision Laboratory,²¹ and the U.S. Naval Research Laboratory (NRL)²²⁻²⁵ programs were important early on. The Canada Centre for Remote Sensing (CCRS) has made numerous airborne and ground-based scatterometer measurements,^{26,27} especially over sea ice. The Environmental Research Institute of Michigan (ERIM),²⁸ CCRS,²⁹ the European Space Agency (ESA),³⁰ and the Jet Propulsion Laboratory (JPL)³¹ used imaging synthetic aperture radars (SARs) for some scattering measurements, but most were not well calibrated. Since the advent of spaceborne SARs (SIR A, B, and C; ERS 1 and 2; Radarsat; Envisat; JERS-1; and others), hundreds of papers have appeared dealing with measurements of scattering and radar applications. Moreover, the JPL AIRSAR has flown around the world, and several other airborne SARs for remote sensing have appeared in various countries, with hundreds of resulting papers. The reader should search the literature for these results, which are far too numerous to reference here. Many of the more recent SARs³²⁻³⁶ also provide information on polarimetric responses.

Results of most of these measurements are summarized in Ulaby, Moore, and Fung³⁷ and Ulaby and Dobson.³⁸ More complete summaries of the earlier work and near-grazing studies are in Long^{22,39} and in the work of Billingsley.¹⁷ Many application summaries are also in the *Manual of Remote Sensing*.^{40,41} Readers requiring more detailed information should consult these books.

16.2 PARAMETERS AFFECTING GROUND RETURN

Radar return depends upon a combination of system parameters and ground parameters:

Radar system parameters (Eqs. 16.1 and 16.2a and b):

- Wavelength
- Power
- Illuminated area
- Direction of illumination (both azimuth and elevation)
- Polarization (including the full polarization matrix when available)

Ground parameters:

- Complex permittivity (conductivity and permittivity)
- Roughness of surface
- Inhomogeneity of subsurface or cover to depth where attenuation reduces waves to negligible amplitude

Different wavelengths are sensitive to different elements on the surface. One of the earliest known and most striking directional effects is the *cardinal-point* effect in returns from cities: Radars looking in directions aligned with primary street grids observe stronger regular returns than radars at other angles. Horizontally polarized waves are reflected better by horizontal wires, rails, etc., than are vertically polarized waves. Vertically polarized waves are reflected better from vertical structures such as tree trunks, at least when the wavelength is comparable or larger than the trunk diameter.

If the geometry of two radar targets were the same, the returns would be stronger from the target with higher complex permittivity because larger currents (displacement or conduction) would be induced in it. Because identical geometries with differing permittivities do not occur in nature, this distinction is not easy to measure. Effective permittivity for ground targets is very strongly influenced by moisture content since the relative permittivity of liquid water is from about 60 at X band to about 80 at S band and longer wavelengths, whereas most dry solids have permittivities less than 8. Attenuation is also strongly influenced by moisture since wet materials usually have higher conductivity than the same materials dry. Figures 16.3 and 16.4 show the effect of moisture content on properties of plants and of soil. The high permittivity of plants with much moisture means that radar return from crops varies as the plants mature, even when growth is neglected.

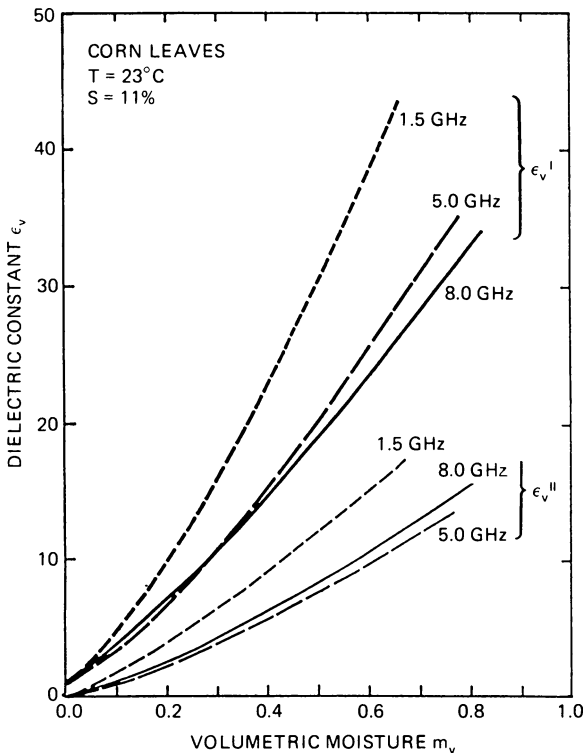


FIGURE 16.3 Measured moisture dependence of the dielectric constant of corn leaves at 1.5, 5.0, and 8.0 GHz. S is the salinity of water content in parts per thousand, $\epsilon_c = \epsilon' - j\epsilon''$ is the complex dielectric constant in Fm^{-1} , and m_v is the volumetric moisture content in kgm^{-3} . (after F. T. Ulaby, R. K. Moore, and A. K. Fung³⁷)

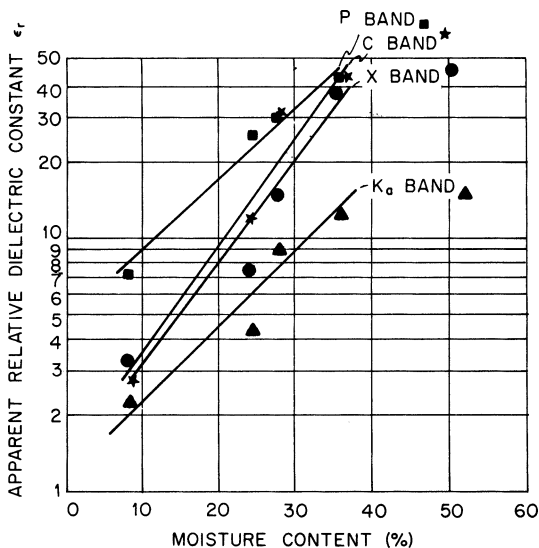


FIGURE 16.4 Apparent relative dielectric constant versus moisture content (Richfield slit loam) (after J. R. Lundien⁴²)

The roughness of surfaces (especially natural ones) is difficult to describe mathematically but easy to understand qualitatively. Thus it is easy to see that a freshly plowed field is rougher than the same field after rain and wind have been at work on it. A forest is inherently rougher than either a field or a city. It is harder to see the difference between the roughness of natural areas and the roughness of a city that has flat walls interspersed with window sills and with curbs, cars, and sidewalks.

Surfaces that are relatively smooth tend to reflect radio waves in accordance with the Fresnel-reflection direction,* so they give strong backscatter only when the look angle is nearly normal to the surfaces. Rough surfaces, on the other hand, tend to reradiate nearly uniformly in all directions, and so they give relatively strong radar returns in any direction.

The problem of radar scatter is complicated because waves penetrate significant distances into many surfaces and vegetation canopies, and internal reflection and scatter contribute to the return. Measurements of attenuation for field crops^{43,44} and grasses⁴⁵ show that most of the return is from the upper layers, with some contribution by the soil and lower layers if the vegetation is not very dense. At C band and higher frequencies, most of the signal returned from trees is usually from the upper and middle branches when the trees are in leaf,^{46–50} although in winter the surface is a major contributor to the signal. At L band, and especially at VHF, the signal penetrates farther, so trunks and the ground can be major contributors even when the trees are leafed out.⁵¹

Additional problems occur near grazing incidence.^{17,52} Because of the low angle with the surface, shadowing frequently occurs—some parts of the target are obscured by intervening projections such as hills and buildings. Parts of the area that are somewhat elevated have the signal modified by the effect of multipath interference between

* Angle of reflection equals angle of incidence.

the direct ray and one reflected off the ground. Since the scattering from relatively level surfaces is very small, any projection may give a return much stronger than the background, thereby skewing the statistics so a Rayleigh distribution no longer applies to the average signal. Objects such as trees, buildings, fence posts, and power lines give localized echoes strong relative to their surroundings.

Moreover, the signal from surfaces without projections falls off very rapidly for depression angles within a few degrees of grazing. This means that the effect of small local slopes can be very significant in modulating the return signal, not just in shadowing.

16.3 THEORETICAL MODELS AND THEIR LIMITATIONS

Descriptions of a Surface. Many theoretical models for radar return from the ground assume a rough boundary surface between air and an infinite homogeneous half space. Some include either vertical or horizontal homogeneities in the ground properties and in vegetative or snow covers.

Surface descriptions suitable for use in mathematical models are necessarily greatly idealized. Few natural grounds are truly homogeneous in composition over very wide areas. Descriptions of their detailed shape must be simplified if they are to be handled analytically, although computers permit the use of true descriptions. Very few surfaces have ever been measured to the precision appropriate for centimeter-wavelength radars; even for these, there is no assurance that scattering boundaries do not exist within a skin depth beneath the surface. Surfaces containing vegetation and conglomerate rocks almost completely defy description.

Statistical descriptions of surfaces are used for most theories, since a theory should be representative of some kind of surface class, rather than of a particular surface, and since exact description is so difficult. The statistical descriptions themselves must be oversimplified, however. Many theories assume isotropic statistics, certainly not appropriate for plowed fields or gridded cities. Most theories assume some kind of model involving only two or three parameters (standard deviation, mean slope, correlation distance, etc.), whereas natural (or human-made) surfaces seldom are so simply described. The theories for vegetation and other volume scatters have more parameters. For near-grazing conditions, the models must account for shadowing.

Simplified Models. Early radar theories for ground return assumed, as in optics, that many targets could be described by a Lambert-law variation of intensity; that is, the differential scattering coefficient varies as $\cos^2 \theta$, with θ being the angle of incidence. This “perfectly rough” assumption was soon found wanting, although it is a fair approximation for the return from many vegetated surfaces over the midrange of angles of incidence.

Clapp¹⁸ described three models involving assemblies of spheres, with different spacings and either with or without a reflecting ground plane. These models yield variations from σ^0 independent of angle through $\sigma^0 \propto \cos \theta$ to $\sigma^0 \propto \cos^2 \theta$. Since the sphere models are highly artificial, only the resulting scatter laws need be considered. Most targets give returns that vary more rapidly over part of the incidence-angle regime than these models, although forests and similar rough targets of some depth sometimes give such slowly varying returns.

Since these rough-surface models usually fail to explain the rise in return near vertical incidence, other simplified models combine Lambert's law and other rough-surface scattering models with specular reflection at vertical incidence, and a smooth curve is drawn between the specular value and the rough-surface prediction.

Specular reflection is defined as reflection from a smooth plane and obeys the Fresnel reflection laws.⁵³ At normal incidence, the specular-reflection coefficient is therefore

$$\Gamma_R = \frac{\eta_g - \eta_0}{\eta_g + \eta_0}$$

where η_0 and η_g are the intrinsic impedances of air and earth, respectively. The fraction of total incident power specularly reflected from a rough surface is⁷

$$e^{-2(2\pi\sigma_h/\lambda)^2}$$

where σ_h = standard deviation of surface height variations, and
 λ = wavelength

Since this proportion is down to 13.5% when $\sigma_h = \lambda/2\pi$ and to 1.8% when $\sigma_h = \lambda/(2\pi\sqrt{2})$, significant specular reflection is seldom found for the centimeter wavelengths generally used for radar. Nevertheless, a simplified model like this is convenient for some purposes.

Observation of reflected sunlight from rippled water, from roads, and from other smooth surfaces leads to the postulation of a facet theory.^{54,55} The only sunlight reaching the observer from smooth surfaces such as water is that from facets for which angle of incidence equals angle of reflection. Thus, the observed light may be described by methods of *geometric optics*.

When geometric optics is used to describe radar scatter, the surface of the ground is represented by small flat-plane segments. Radar return is assumed to occur only for facets oriented normal to the radar (normal orientation is required for backscatter so that the reflected wave returns to the source). Thus, if the slope distribution of such facets is known, the fraction normal to a given diverging beam can be established, and from this the return can be obtained. Geometric optics assumes zero wavelength, and so the results of such a theory are wavelength-independent, clearly not in accord with observation.

The facet model for radar return is extremely useful for qualitative discussions, and so modification to make it fit better with observation is appropriate. Two kinds of modification may be used, separately or jointly: considering the actual reradiation pattern of finite-size facets at finite wavelengths⁵⁵ and considering the effect of wavelength on establishing the effective number of facets.⁵⁶ Thus, the scatter from a facet may actually occur in directions other than that requiring that angle of incidence equal angle of reflection. Figure 16.5 illustrates this. For large facets (compared with wavelength), most of the return occurs almost at normal incidence, whereas for small facets the orientation may be off normal by a considerable amount without great reduction in scatter. As the wavelength is increased, the category of a given facet changes from *large* to *small*; eventually the facet is smaller than a wavelength, and its reradiation pattern shape remains almost isotropic from that point. Many facets that would be separate at, say, a 1-cm wavelength are combined at a 1-m wavelength; the result may be a transition from rough- to smooth-surface behavior. Figure 16.6a shows a number of facets of different sizes contributing to a radar return.

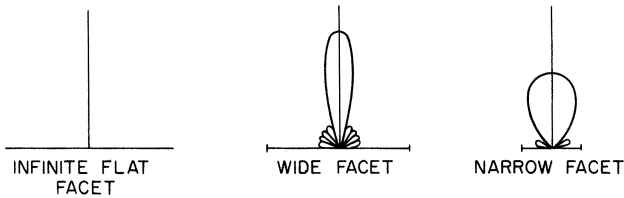


FIGURE 16.5 Normal-incidence reradiation patterns of facets

Physical Optics Models. Theories based on applications of the Kirchhoff-Huygens principle have been thoroughly developed.^{37,55,57-59} The Kirchhoff approximation is that the current flowing at each point in a locally curved (or rough) surface if it were flat and oriented tangent to the actual surface. This assumption permits construction of scattered fields by assuming that the current over a rough plane surface has the same magnitude as if the surface were smooth, but with phase perturbations set by the differing distances of individual

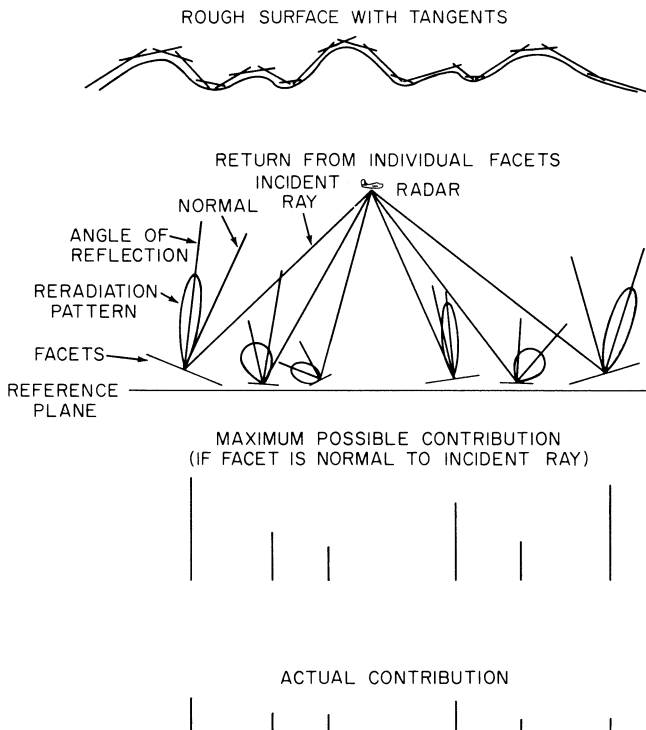


FIGURE 16.6a Facet model of a radar return

points from the mean plane. For surfaces assumed to be azimuthally isotropic, the usual approach yields integrals of the form

$$\frac{1}{\cos^3 \theta} \int e^{-(2k\sigma_h \cos \theta)^2 [1-\rho(\xi)]} J_0(2k\xi \cos \theta) \xi d\xi$$

where $\rho(\xi)$ = spatial autocorrelation function of surface heights
 θ = angle with vertical
 σ_h = standard deviation of surface heights
 $k = 2\pi/\lambda$
 J_0 = first-order, first-kind Bessel function

The autocorrelation function of height with distance is seldom known for terrain, although it can be determined on a large scale by analysis of contour maps,⁶⁰ and it has been found for some areas by careful contouring at close intervals and subsequent analysis. Because of lack of knowledge of actual autocorrelations, most theory has been developed with artificial functions that are chosen more for their integrability than for their fit with nature; selection among them has been on the basis of which ones yield the best fit between theoretical and experimental scatter curves.

The correlation function first used⁶¹ was gaussian:

$$\rho(\xi) = e^{-\xi^2/L^2} \quad (16.5)$$

where L is the *correlation length*. Not only is this a function that makes the integral analytically tractable, but it also gives exactly the same results as geometric optics.⁶² Since it fails, like geometric optics, to explain frequency variation, it cannot be a truly representative correlation function, although it gives a scattering curve that fits several experimental curves near the vertical. The next most frequently used function is the exponential:

$$\rho(\xi) = e^{-|\xi|/L} \quad (16.6)$$

This has some basis in contour-map analysis;⁶⁰ the results fit both Earth and lunar radar return over a wider range of angles than the gaussian^{60,63} (but sometimes not as well near vertical). Furthermore, it has the merit that it exhibits frequency dependence. Resulting expressions for power (scattering coefficient) variations appear in Table 16.1.

TABLE 16.1 Scattering Coefficient Variation

Correlation coefficient	Power Expression	Reference
$e^{-\xi^2/L^2}$	$\frac{K}{\sin \theta} e^{-(L^2/2\sigma_h^2) \tan^2 \theta}$	Davies ⁶¹
$e^{- \xi /L}$	$\frac{K\theta}{\cos^2 \theta \sin \theta} \left(1 + A \frac{\sin^2 \theta}{\cos^4 \theta} \right)^{-3/2}$	Voronovich ⁵

Small-Perturbation and Two-Scale Models. Recognition that existing models were inadequate for describing ocean scatter led to recognition that resonance of the signal with small structures on the surface has a powerful influence on the strength of the signal received.^{64,65} Thus a small-perturbation method originally proposed by Rice⁶⁶ became the most popular way to describe ocean scatter. Its application to land scatter was not far behind.

The term *Bragg scatter* is often used to describe the mechanism for the small-perturbation model. The idea comes from the concept illustrated in Figure 16.6b.

A single sinusoidal component of a complex surface is shown with an incoming radar wave at angle of incidence θ . The radar wavelength is λ , and the surface-component wavelength is Λ . When the signal travels an extra distance $\lambda = 2\Delta R$ between the source and two successive wave crests, the phase difference between the echoes from successive crests is 360° ; so the echo signals all add in phase. If this condition is satisfied for a particular Λ and θ , it fails to be satisfied for others. Thus, this is a resonant selection for a given θ of a particular component of the surface Λ . The strength of the received signal is proportional to the height of this component and to the number of crests illuminated by the radar. If the surface has an underlying curvature, the number of illuminated crests satisfying the resonance criterion may be limited by the length of the essentially flat region; otherwise, it is limited by the radar resolution.

The theoretical expression for the scattering coefficient is⁶⁷

$$\sigma_{pq}^0 = 8k^4 \sigma_1^2 \cos^4 \theta |\alpha_{pq}|^2 W(2k \sin \theta, 0) \quad (16.7)$$

where p, q = polarization indices (H or V)

$k = 2\pi/\lambda$ (the radar wavenumber)

$\alpha_{HH} = R_1$ (Fresnel reflection coefficient for horizontal polarization)

$$\alpha_{VV} = (\epsilon_r - 1) \frac{\sin^2 \theta - \epsilon_r (1 + \sin^2 \theta)}{[\epsilon_r \cos \theta + (\epsilon_r - \sin^2 \theta)^{1/2}]^2}$$

where ϵ_r is the relative permittivity $\epsilon' - j\epsilon''$ and $\alpha_{VH} = \alpha_{HV} = 0$. $W(2k \sin \theta, 0)$ is the *normalized roughness spectrum* (the Fourier transform of the surface autocorrelation function). It may be written as $W(K, 0)$, where K is the wavenumber for the surface. In terms of the wavelength on the surface Λ ,

$$K = 2\pi/\Lambda$$

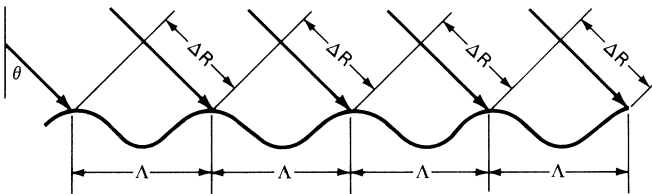


FIGURE 16.6b In-phase addition for Bragg scattering: $\Delta R = n\lambda/2$

Thus, the component of the surface that satisfies the Bragg resonance condition is

$$\Lambda = \lambda/2 \sin \theta \quad (16.8)$$

This means that the most important contributor to a surface return is the component of surface roughness with wavelength Λ . Even though other components may be *much* larger, the Bragg resonance makes this component more important. On the ocean, this means that tiny ripples are more important than waves that are meters high; the same applies for land-surface scatter.

As originally developed, this theory was for perturbations to horizontal flat surfaces, but it was soon modified to handle surfaces with large-scale roughness. The large-scale roughness was assumed to cause a *tilting* of the flat surface to which the small-perturbation theory could be applied. The principal problem with this approach is deciding where in the surface spectrum lies the boundary between the larger components that do the tilting and smaller components that are Bragg-resonant. Many papers have been written to describe the evolution of this theory; for a complete summary, the reader is referred to Fung's development.⁶⁸

Other Models. The theory for volume scatter has led to many papers and continues to evolve. For a review of some of the approaches, the reader should consult Fung's summary⁶⁹ and papers by Kong, Lang, Fung, and Tsang. These models have been used reasonably successfully to describe scatter from vegetation,⁷⁰ snow,⁷¹ and sea ice.⁷² Models of straight vegetation such as wheat in terms of cylinders have had some success.^{2,73} Corner-reflector effects have been used to describe strong returns from buildings at non-normal incidence angles.^{74,75} Other specialized models have been used for particular purposes.

Later theoretical work for surfaces involves solving integral equations for the scattered fields.⁷⁶ This has been used both to validate other models and to better describe the true scattering from a known rough surface. This method tends to be computationally extensive. Numerical scattering computations are also in vogue.⁷⁷

Regardless of the model used and the approach applied to determining the field strength, theoretical work only guides understanding. Actual Earth surfaces are too complex to be described adequately in any of the models, and the effects of signals that penetrate the ground and are scattered therein are too little known to permit its evaluation.

16.4 FADING OF GROUND ECHOES

The amplitude of ground echoes received by radars on moving vehicles fluctuates widely because of variations in phase shift for return from different parts of the illuminated area. In fact, even fixed radars frequently observe fluctuations in ground echoes because of motions of vegetation, wires blowing in the wind, etc. This fluctuation is referred to as *fading*.

Fading is significant for the radar engineer because one must account for the fact that a single sample of the radar return may vary widely from the mean described by σ^0 . Thus, the system must be able to handle the dynamic range of fading, which may exceed 20 dB.

Regardless of the model used to describe a ground surface, signals are, in fact, returned from different positions not on a plane. As a radar moves past a patch of ground

while illuminating it, the look angle changes, and this changes the relative distances to different parts of the surface; the result is that relative phase shift is changed. This is the same kind of relative-phase-shift change with direction that is present for an antenna array and results in the antenna pattern. For ground echo, the distance is doubled, so the pattern of an echoing patch of length L has lobes of width $\lambda/2L$. This compares with λ/L for an antenna of the same cross-range length. Because the excitation of the elements of the scattering array is random, the scattering pattern in space is also random.

This fading phenomenon is usually described in terms of the doppler shift of the signal. Since different parts of the target are at slightly different angles, the signals from them experience slightly different doppler shifts. The doppler shift, of course, is simply the rate of change of phase due to motion. Thus, the total rate of change of phase for a given target is

$$\omega = \omega_c + \omega_{di} = \frac{d\phi_i}{dt} = \frac{d}{dt}(\omega_c t - 2kR_i) \quad (16.9)$$

where ω_c = carrier angular frequency

ω_{di} = doppler angular frequency for i th target

ϕ_i = phase for i th target

R_i = range from radar to i th target

The doppler shift can be expressed in terms of the velocity vector \mathbf{v} as

$$\omega_{di} = -2k \frac{dR_i}{dt} = -2k\mathbf{v} \cdot \frac{\mathbf{R}_i}{R_i} = -2k\mathbf{v} \cos(\mathbf{v}, \mathbf{R}_i) \quad (16.10)$$

where bold-faced letters are vectors. Hence, the total field is given by

$$E = \sum_i A_i \exp \left\{ j \left[\omega_c t - \int_0^t 2k\mathbf{v} \cdot \frac{\mathbf{R}_i}{R_i} dt - 2kR_{i0} \right] \right\} \quad (16.11)$$

where A_i is the field amplitude of the i th scatterer and R_{i0} is the range at time zero.

The only reason the scalar product varies for different scatterers is the different angle between the velocity vector and the direction to the scatterer. This results in a separate doppler frequency for each scatterer. If we assume the locations to be random, as most theories do, the received signal is the same as one coming from a set of oscillators with random phases and unrelated frequencies. This same model of a group of randomly phased, different-frequency oscillators is used to describe noise; *thus, the statistics of the fading signal and the statistics of random noise are the same.*

This means that the envelope of the received signal is a random variable with its amplitude described by a Rayleigh distribution. Such distributions have been measured for many ground-target echoes.²³ Although the actual distributions vary widely, no better description can be given for relatively homogeneous targets. With a Rayleigh distribution, the 90% range of fading is about 18 dB, so an individual pulse return may be anywhere in this range.

When a target is dominated by one large echo (such as a metal roof oriented to give a strong return), the distribution is better described by that for a sine wave in noise. If the large echo is considerably stronger than the mean of the remaining contributors to the return, this approaches a normal distribution about the value for the large echo. This situation is particularly common for near-grazing conditions.¹⁷

For reference, the two distributions are given⁷⁸:

$$p(v) dv = \frac{v}{\psi_0} e^{-v^2/2\psi_0} dv \quad (\text{Rayleigh})$$

$$p(v) dv = \frac{v}{\psi_0^{1/2}} e^{-(v^2+a^2)/2\psi_0} I_0\left(\frac{av}{\psi_0}\right) \quad (\text{sine wave} + \text{Rayleigh})$$

where v = envelope voltage

ψ_0 = mean square voltage

A = sine-wave peak voltage

$I_0(x)$ = Bessel function, first kind, zero order, imaginary argument

In practice, the distribution from large targets may be more complicated than either of the simple models described. Indeed, particularly near grazing incidence, the signal is often described by a K , a Weibull, or a log-normal distribution.⁷⁹⁻⁸¹ These distributions are more often used to describe the variations between different returns from an area, rather than fading. They may be thought of as describing what happens when the area contains different σ^0 s, and the distribution for each is Rayleigh. Because of this, the range of variability may be even greater than the 18 dB for a Rayleigh distribution.

Fading-Rate Computations. Doppler frequency calculation is the easiest way to find fading rates. To compute the signal amplitude returned with a particular range of doppler shifts, all signals having such shifts must be summed. This requires knowing the contours of constant doppler shift (isodops) on the scattering surface. These contours must be established for each particular geometric arrangement. A simple example is presented here: horizontal motion over a plane earth. This is typical of an aircraft in ordinary cruising flight.

Consider travel in the y direction, with z vertical and the altitude (fixed) $z = h$. Then

$$\mathbf{v} = \mathbf{1}_y v$$

$$\mathbf{R} = \mathbf{1}_x x + \mathbf{1}_y y + \mathbf{1}_z h$$

where $(\mathbf{1}_x, \mathbf{1}_y, \mathbf{1}_z)$ are unit vectors. Hence,

$$v_r = \mathbf{v} \cdot \frac{\mathbf{R}}{R} = \frac{vy}{\sqrt{x^2 + y^2 + h^2}}$$

where v_r is the relative speed. Curves of constant relative speed are also curves of constant doppler shift. The equation of such a curve is

$$x^2 - y^2 \frac{v^2 - v_r^2}{v_r^2} + h^2 = 0$$

This is a hyperbola. The limiting curve for zero relative speed is a straight line perpendicular to the velocity vector. Figure 16.7 shows such a set of constant-doppler-shift contours.

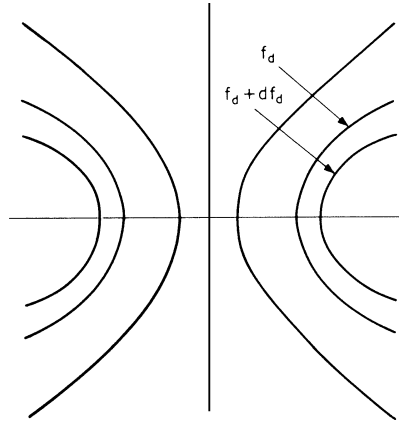


FIGURE 16.7 Contours of constant doppler frequency shift on a plane earth due to horizontal motion

The spectrum of fading can be calculated by a slight rearrangement of the radar equation (Eq. 16.1). Thus, if $W_r(f_d)$ is the power received between frequencies f_d and $f_d + df_d$, the radar equation becomes

$$W_r(f_d) df_d = \frac{1}{(4\pi)^2} \int_{\text{Illuminated area between } f_d \text{ and } f_d + df_d} \frac{P_t G_t A_r \sigma^0 dA}{R^4} = \frac{df_d}{(4\pi)^2} \int \frac{P_t G_t A_r \sigma^0}{R^4} \left(-\frac{dA}{df_d} \right) \quad (16.12)$$

This is an integral in which the area element between f_d and $f_d + df_d$ is expressed in terms of coordinates along and normal to the isodops. Such coordinates must be established for each particular case.

Figure 16.8 shows the geometry for horizontal travel. The coordinate ξ is along the isodop, and η is normal to it. We can express Eq. 16.12 in terms of these coordinates as

$$W_r f_d = \frac{d\eta}{df_d} \left[\frac{\lambda^2}{(4\pi)^3} \right] \int_{\text{strip}} \left[\frac{P_t G^2 \sigma^0 d\xi}{R^4} \right] \quad (16.13)$$

Note that P_t , the transmitted power, is non-zero in the integral only for the time it illuminates the ground. In pulse radars, only that part of the ground area providing signals back to the radar at a particular time can be considered to have finite P_t , and so the range of frequencies that can be present is limited by the pulse, as well as by the antennas and the maximum velocity.

Another example is shown in Figure 16.9. This is the small illuminated area for a narrow-beam short-pulse system with the antenna pointed straight ahead. Here, we can make linear approximations without too much error.

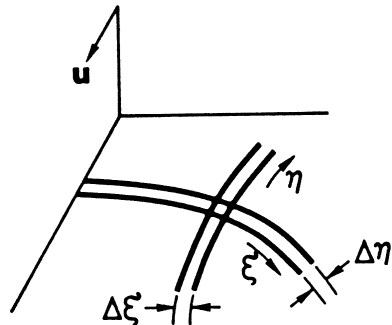


FIGURE 16.8 Geometry of complex fading calculations (after F. T. Ulaby, R. K. Moore, and A. K. Fung³⁷)

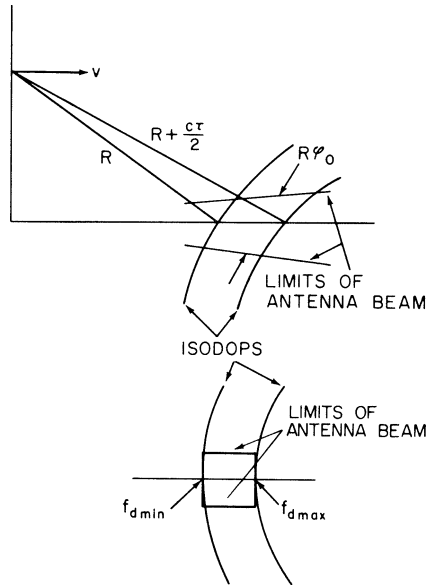


FIGURE 16.9 Geometry of doppler-shift calculations for an airborne search radar

A pulse of length τ is transmitted from an antenna of beamwidth ϕ_0 . We may simplify the problem by assuming a rectangular illuminated area, $R\phi_0 c\tau/(2 \sin \theta)$. Furthermore, the curvature of the isodops may be neglected, so the doppler frequency is assumed to be the same for all maximum-range points and the same for all minimum-range points. With this assumption,

$$f_{d \max} = \frac{2v}{\lambda} \sin \theta_{\max}$$

$$f_{d \min} = \frac{2v}{\lambda} \sin \theta_{\min}$$

Thus, the total width of the doppler spectrum is

$$\Delta f_d = \frac{2v}{\lambda} (\sin \theta_{\max} - \sin \theta_{\min})$$

For short pulses and angles away from vertical, this is

$$\Delta f_d \approx \frac{2v}{\lambda} \Delta \theta \cos \theta$$

In terms of pulse length, it becomes

$$\Delta f_d = \frac{vc\tau}{2h\lambda} \frac{\cos^3 \theta}{\sin \theta} \quad (16.14)$$

If the angular difference across the illuminated rectangle is small enough so that σ^0 is essentially constant, the doppler spectrum is a rectangle from f_{\min} to f_{\max} .

In practice, antenna beams are not rectangular. The result is that the doppler spectrum for a side-looking radar like that shown in the example is not rectangular but rather has the shape of the antenna along-track pattern. Thus, if the antenna pattern in the along-track direction is $G = G(\beta)$, with β the angle off the beam center, we can express β in terms of the doppler frequency f_d as

$$\beta = f_d \lambda / 2v$$

and the spectrum is

$$W(f_d) = \frac{\lambda^3 P_t \sigma^0 r_x}{2(4\pi)^3 R^3} G^2 \left[\frac{\lambda f_d}{2v} \right]$$

where r_x is the horizontal resolution in the range direction. Of course, the half-power beamwidth may be used as an approximation, resulting in the bandwidth given by Eq. 16.13.

Effect of Detection. The effect of detecting narrowband noise has been treated extensively in the literature. Here, it is necessary only to show the postdetection spectrum of the preceding example and to consider the number of independently fading samples per second. Figure 16.10 shows the spectrum before and after square-law detection. For square-law detection, the post-detection spectrum is the self-convolution of the predetection spectrum. Only the part that passes the low-pass filters in a detector is shown in the figure. The rectangular *RF spectrum* has become a triangular *video spectrum*.

This spectrum describes the fading of the detector output for a CW radar. For a pulse radar, the spectrum is sampled by the pulse repetition frequency (PRF). If the PRF is high enough so that the entire spectrum can be reproduced (the PRF is higher than the Nyquist frequency, $2\Delta f_d$), the diagram indicated is that of the spectrum of the samples of a received pulse at a given range. Figure 16.11 shows a series of actual pulses from a moving radar, followed by a series of samples at range R_1 . The spectrum shown in Figure 16.10 is the spectrum of the envelope of samples at R_1 (after low-pass filtering). The spectrum of fading at another range (or vertical angle) is different, in accord with Eq. 16.13.

For many purposes, the number of *independent* samples is important because these may be treated by using the elementary statistics of uncorrelated samples. For continuous integration, the effective number of independent sample is⁷⁸

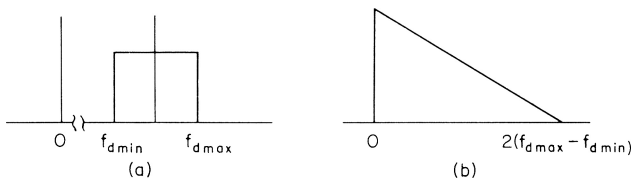


FIGURE 16.10 Spectrum of fading from a homogeneous small patch (a) before and (b) after detection

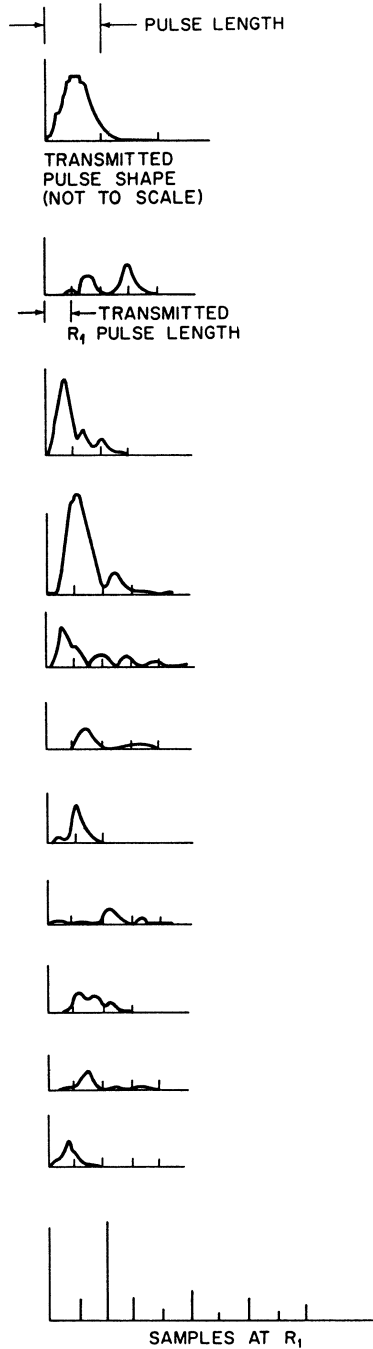


FIGURE 16.11 Fading for successive pulses of a moving radar with ground target

$$N = \frac{\overline{P_e^2} T}{2 \int_0^T \left[1 - \frac{x}{T} \right] R_{sf}(x) dx} \quad (16.15)$$

where $\overline{P_e}$ is the mean envelope power, T is the integration (averaging) time, and $R_{sf}(t)$ is the autocovariance function for the detected voltage. For many practical purposes, if N is large, it may be approximated by

$$N \approx BT \quad (16.16)$$

where B is the effective IF bandwidth. For the effect of short integration time, see Ulabay et al.⁸²

Fading samples can, of course, also be independent because motion of the vehicle causes the beam to illuminate a different patch of ground. Thus, in a particular case, the independent-sample rate may be determined either by the motion of the illuminated patch over the ground or by the doppler effect or by some combination of the two.

The number of independent samples determines the way in which the Rayleigh or other distributions may be applied. Thus, if 100 pulses give only 10 independent samples, the variance of the mean obtained by integrating these pulses is much greater than would be true if all 100 pulses were independent.

Doppler-based systems, such as doppler navigators, moving-target indicators, and synthetic-aperture radar systems, depend on the predetection spectrum for their operation, because they are coherent and do not use amplitude or square-law detection.

Moving-Target Surfaces. Sometimes clutter has internal motion. This can occur when fixed radars are used to observe movement of the sea and the land. On land, clutter motion is usually due to moving vegetation, although moving animals and machines create similar effects. The radar return from an assembly of scatterers like those shown in Figure 16.8 can change because of motion of the individual scatterers just as it changes because of motion of the radar. Thus, if each scatterer is a tree, the waving of the trees as the wind blows causes relative phase shifts between the separate scatterers; the result is fading. For a fixed radar, this may be the only fading observed, except for very slow fading due to changes in refraction. If the surface elements are stiff, they may not move enough to get significant doppler spreading, and the fading distribution may not be close to Rayleigh. See Billingsley¹⁷ and other papers by him for more discussion of the situation for fixed radars observing ground targets. For a moving radar, this motion of the target changes the relative velocities between target element and radar so that the spectrum is different from that for a fixed surface. The width of the spectrum due to vehicle motion determines the ability of the radar to detect this target motion.

16.5 MEASUREMENT TECHNIQUES FOR GROUND RETURN

Special-purpose instrumentation radars and modified standard radars may be used to determine the ground return. Since the ground return is almost invariably due to scattering, these systems are termed *scatterometers*. Such systems may use CW signals with or without doppler processing, but they may also use both pulse and FM techniques.

Scatterometers capable of measuring response over a wide range of frequencies are called *spectrometers*.⁸³ Various antenna patterns from pencil beams to fan beams may be used. Systems to measure the full polarization matrix must use very careful antenna designs so that the phases of the different transmitted and received polarizations are well controlled, and leakage between polarizations is thoroughly suppressed.

CW and FM-CW Systems. The simplest scatterometer uses a stationary CW radar. Such systems are not very flexible, but they are discussed here in some detail to illustrate calibration techniques that also apply to the more complex systems.

The CW scatterometer is shown in block form in Figure 16.12. To evaluate σ^0 the ratio of transmitted to received power is required. The system depicted in Figure 16.12a measures transmitter power and receiver sensitivity separately. The transmitter feeds an antenna through a directional coupler so that a portion of the energy may be fed to a power meter. The receiver operates from a separate antenna (electrically isolated). The output of the receiver is detected, averaged, and digitally recorded. Its sensitivity must be checked by use of a calibration source. The calibrated signal may be fed through the receiver at a time when the transmitter is off. Figure 16.12b shows a similar arrangement in which the signal from the transmitter is attenuated a known amount and used to check the receiver gain. By comparing the output from the attenuated transmitter signal with that received from the ground, the scattering cross section may be determined without actually knowing the transmitted power and the receiver gain.

The calibrations shown in Figure 16.12 are incomplete without knowing the antenna patterns and absolute gains. Since accurate gain measurements are difficult, absolute calibrations may be made by comparing received signals (with proper relative calibration) from the target being measured and from a *standard target*. Standard targets may be metal spheres, Luneburg-lens reflectors, metal plates, corner reflectors, or active radar calibrators (ARCs—actually repeaters).^{84,85} Of the passive calibrators, the Luneburg-lens reflector is best because it has a large cross section for its volume and has a very wide pattern so that alignment is not critical. Luneburg-lens reflectors are used for making strong radar targets of small vessels, and they may be obtained

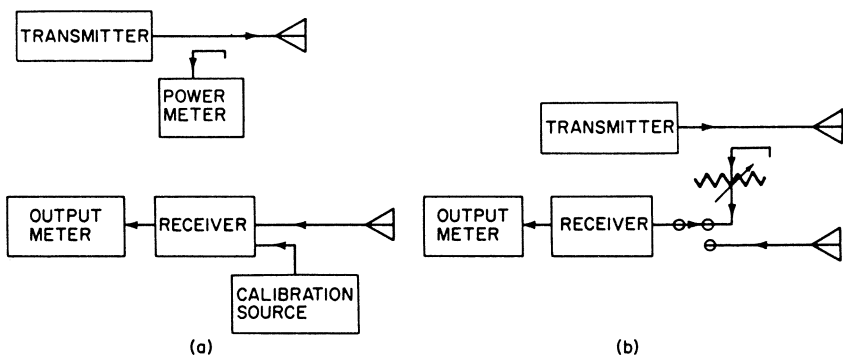


FIGURE 16.12 CW-scatterometer-system block diagram: (a) separate transmitter and receiver calibration and (b) calibration of the ratio of received to transmitted power

from companies that supply that market. For discussion of the relative merits of different passive calibration targets, see Ulaby et al.⁸⁶

The ideal receiver would respond linearly to its input, so that a single calibration at one input level would suffice for all levels. The usual receiver, however, has some nonlinearities due to detector properties and to saturation of its amplifiers by large signals. Figure 16.13 shows a typical input-output curve for a receiver. Two equal increments in input signal (Δ^i), as shown, produce different increments in output because of the nonlinearity of this curve. For this reason, receiver calibration must be performed over a range of input levels, and the nonlinearities must be compensated for in the data processing.

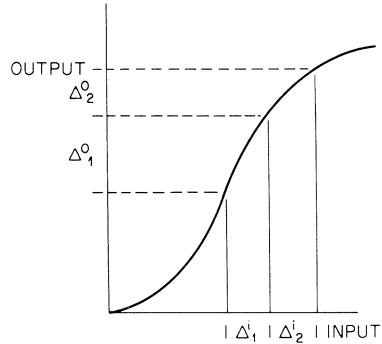


FIGURE 16.13 Typical receiver input-output curve. Illustrated is the effect of nonlinearity.

CW scatterometers depend on antenna beams to discriminate different angles of incidence and different targets. Usually assumptions are made that the antenna pattern has constant gain within the actual 3 dB points and zero gain outside, but this clearly is not an accurate description. If large targets appear in the locations illuminated by the side of the main beam or the minor lobes, their signals may contribute so much to the return that it is significantly changed. Since this changed signal is charged to the direction of the major lobe by the data reduction process, the resulting value for σ^0 is in error. Responses at vertical incidence frequently cause trouble, for vertical-incidence signals are usually fairly strong. Thus the antenna pattern must be accurately known and taken into account in the data analysis. A pattern with strong minor lobes may be simply inadmissible.

The scattering coefficient is determined by applying

$$P_r = \frac{P_i \lambda^2}{(4\pi)^3} \int_{\text{illuminated area}} \frac{G_i^2 \sigma^0 dA}{R^4}$$

The integration is over whatever area is illuminated significantly, including the regions hit by the minor lobes. The usual assumption is that σ^0 is constant over the illuminated area, so that

$$P_r = \frac{P_i \lambda^2 \sigma^0}{(4\pi)^3} \int_{\text{illuminated area}} \frac{G_i^2 dA}{R^4} \quad (16.17)$$

This assumption would be true only if the antenna confined the radiated energy to a very small spread of angles and to a fairly homogeneous region. The resulting expression is

$$\sigma^0 = \frac{(4\pi)^3 P_r}{P_i \lambda^2 \int_{\text{illuminated area}} (G_i^2 / R^4) dA} \quad (16.18)$$

Note that only the ratio of transmitted to received power is required, so the technique shown in Figure 16.12*b* is justified. Sometimes R , G_r , or both are assumed constant over the illuminated area, but such an approximation to Eq. 16.18 should be attempted only after checking its validity for a particular problem.

If the result of applying the technique of Eq. 16.18 to a set of measurements indicates that σ^0 probably did vary across the significantly illuminated area, this variation may be used as a first approximation to determine a function $f(\theta)$ describing the θ variation of σ^0 , and a next-order approximation then becomes

$$\sigma^0 = \frac{(4\pi)^3 P_r}{P_t \lambda^2 \int_{\text{illuminated area}} [f(\theta) G_t^2 / R^4] dA} \quad (16.19)$$

Proper scattering measurements demand an accurate and complete measurement of antenna gain G_r . This can be a very time-consuming and expensive process, particularly when the antenna is mounted on an aircraft or other metallic object. Nevertheless, complete patterns are a must for good scatter measurements.

Range-Measuring Systems. Radar's ability to separate returns from different ranges can be used advantageously along with directive antenna beams to simplify the scattering measurements. Most ranging scatterometers use either pulse modulation or FM, although more exotic modulations could also be used. The discussion here treats pulse systems, but since all other range-measuring systems can be reduced to equivalent pulse systems, most results are general.

Figure 16.14 shows the way in which pulse measurement of range is used. Figure 16.14*a* shows a circular pencil beam. At angles near grazing, the illuminated patch set by the circular antenna pattern becomes rather long (the patch is an ellipse), and use of the pulse length to confine illumination to a part of the patch is helpful. Indeed, for angles very near grazing, this is the only satisfactory way to resolve small regions. Many systems that use beamwidth to set the measured area near vertical use range resolution for angles beyond, say, 60° .

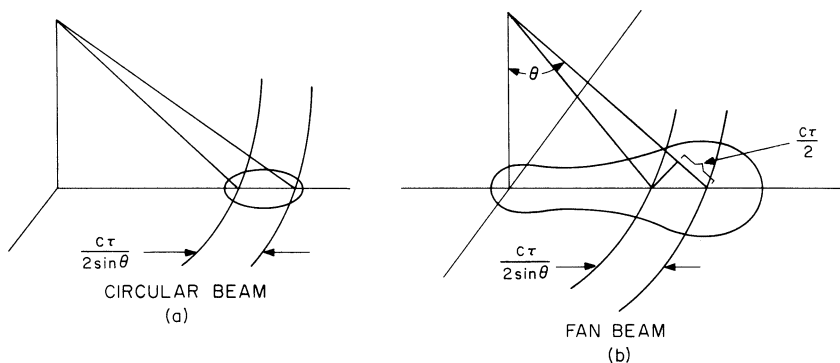


FIGURE 16.14 Range resolution applied to scatterometry: (a) improving one dimension of a circular-beam illumination pattern and (b) use with a fan beam

Figure 16.14*b* shows an antenna pattern that takes better advantage of the possibilities of range measurement. A fan beam is used to illuminate a narrow strip along the ground, and the range resolution permits separating the returns from different angles by the time they return. This technique is especially effective at angles away from the vertical, for the resolution near the vertical is much poorer than near grazing.

If we assume that σ^0 is essentially constant, the gain is constant, the pulse is rectangular, and the difference in range across a resolution element is negligible, the expression for σ^0 becomes

$$\sigma^0 = \frac{P_r (4\pi)^3 R^3 \sin \theta}{P_t \lambda^2 G_0 \phi_0 r_R} \quad (16.20)$$

where r_R is the short-range resolution.

Janza has reported details of calibration problems with a range-measuring pulsed radar scatterometer.^{87,88}

CW-Doppler Scatterometers. A convenient way for an airborne measurement is to measure the scattering coefficient at many angles simultaneously with a CW system in which the relative velocities corresponding to different angles are separated by separating their doppler frequencies. The use of a fan beam with such a system permits the simultaneous measurement of scattering coefficients at points ahead of and behind the aircraft carrying the radar. Figure 16.15 shows this. The pattern of the antenna illumination on the ground is shown intersected by two isodops (lines of constant doppler frequency), with the width of the spectrum between them shown on the diagram. The distance between them can be seen to be

$$\Delta \rho = R(\sin \theta_2 - \sin \theta_1)$$

and

$$\Delta f_d = \frac{2v}{\lambda} (\sin \theta_2 - \sin \theta_1)$$

Thus, the width of the element on the ground is related to the doppler frequency bandwidth by

$$\Delta \rho = \frac{R\lambda}{2v} (\Delta f_d)$$

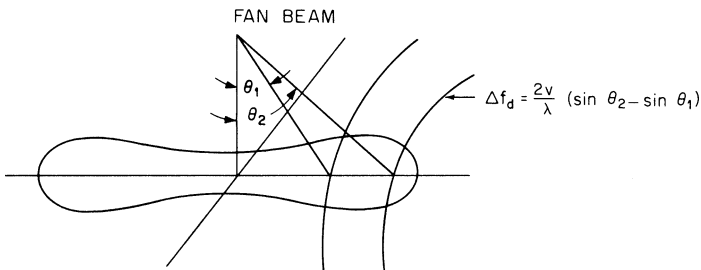


FIGURE 16.15 Resolution in a fan-beam CW-doppler scatterometer

where this technique is applied to the radar equation and the following are assumed:

1. σ^0 constant in the illuminated area
2. Antenna gain constant over its beamwidth Φ and zero elsewhere
3. Range variation across the small illuminated area negligible

$$P_r = \frac{P_t \lambda^2}{(4\pi)^3} \int \frac{G^2 \sigma^0 dA}{R^4} = \frac{P_t \lambda^4 \sigma^0 G_0^2 \Phi \Delta f_d}{2vR^2} \quad (16.21)$$

and so

$$\sigma^0 = \frac{P_r}{P_t} \frac{2vR}{\lambda^4 G_0^2 \Phi \Delta f_d} \quad (16.22)$$

Doppler scatterometers need not use fore-and-aft beams. The Seasat⁸⁹ and NSCATT⁹⁰ spaceborne doppler scatterometers were designed with beams pointed (squared) ahead and behind the normal to the ground track.

Independent Samples Required for Measurement Accuracy. The Rayleigh distribution describes the fading signal fairly well. If we assume a Rayleigh distribution of fading, the number of independent samples required for a given accuracy is shown in Figure 16.16. The *range* defined in this figure is the range of mean values lying between 5 and 95% of points on the distribution. This accuracy range is independent of any accuracy problems associated with calibration and knowledge of the antenna pattern.

The precision of the measurement depends upon the number of *independent* samples, not on the total number of samples. The number of independent samples can be found from Eq. 16.15 or Eq. 16.16 after suitable analysis. This analysis assumes that only doppler fading contributes to independence but motion from one cell to another also adds independent samples. Thus, the total number of such samples is approximately the product of the number calculated from Eq. 16.13 and the number of ground cells averaged. Figure 16.17 shows some examples of the effect of the angle of incidence on the number of independent samples for a horizontally traveling scatterometer with a forward-pointed beam.

Study of the results obtained in this type of analysis indicates that, in regions where the scattering coefficient does not change rapidly with angle, the widest possible angular width (obtained by a longer pulse or a wider filter for a CW-doppler system) gives the maximum number of independent samples for a given distance traveled along the ground.

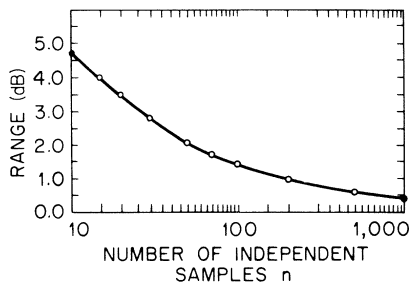


FIGURE 16.16 Accuracy of averages for fading signals

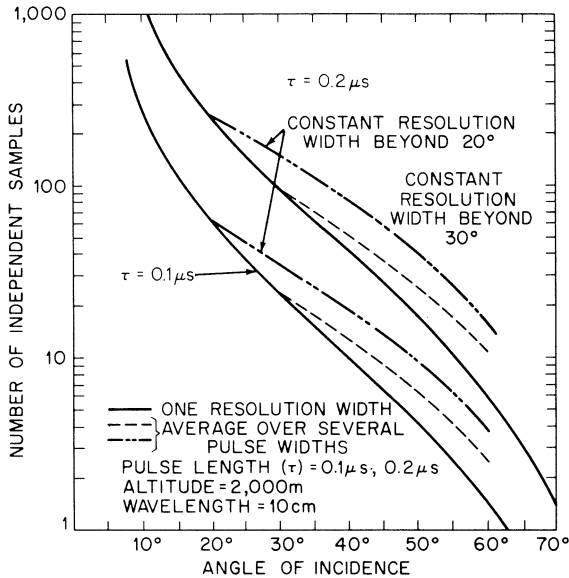


FIGURE 16.17 Examples of the variation with angle of incidence of the number of independent samples for a scatterometer

Near-Vertical Problem. Most published radar return data purporting to include vertical incidence give vertical-incidence scattering coefficients that are too small. This is a consequence of a fundamental problem in measuring near the vertical with a finite beamwidth or pulse length. Near-vertical radar returns from most targets drop off rapidly as the angle with the vertical is increased. Thus, the measuring beamwidth or pulsewidth usually encompasses signals from regions having values for σ^0 many decibels apart. Since the scattering coefficient varies much more rapidly near the vertical than at angles beyond 10 or 20° from the vertical, the problem is much more severe at the vertical. Furthermore, the problem is complicated at the vertical by the fact that the angular scale terminates there, so that a beam centered at the vertical illuminates weaker targets (σ^0) on both sides of its pattern, whereas a beam away from the vertical illuminates stronger signals on one side and weaker signals on the other.

Figure 16.18 shows what happens for a steeply descending curve of σ^0 versus θ . The radar return integral from Eq. 16.1 is a convolution integral; the figure shows the convolution of the beam pattern with the σ^0 curve. Clearly, the average at the vertical is lower than it should be to indicate properly the variation of σ^0 near the vertical.

Figure 16.19 shows an example⁹¹ based on the theoretical scattering coefficient for the sea derived from the spectra reported by the Stereo Wave Observation Project.⁹² The effect of different beamwidths is clearly shown.

With a pulse or other range-measuring system, reported values are always in error because, as indicated above, it is almost impossible to resolve a narrow range of angles near the vertical. For short ranges, one can configure the antenna so that a plane wave impinges on the surface. When this is done, the near-vertical scattering coefficient can have its angular variation properly described.⁹³

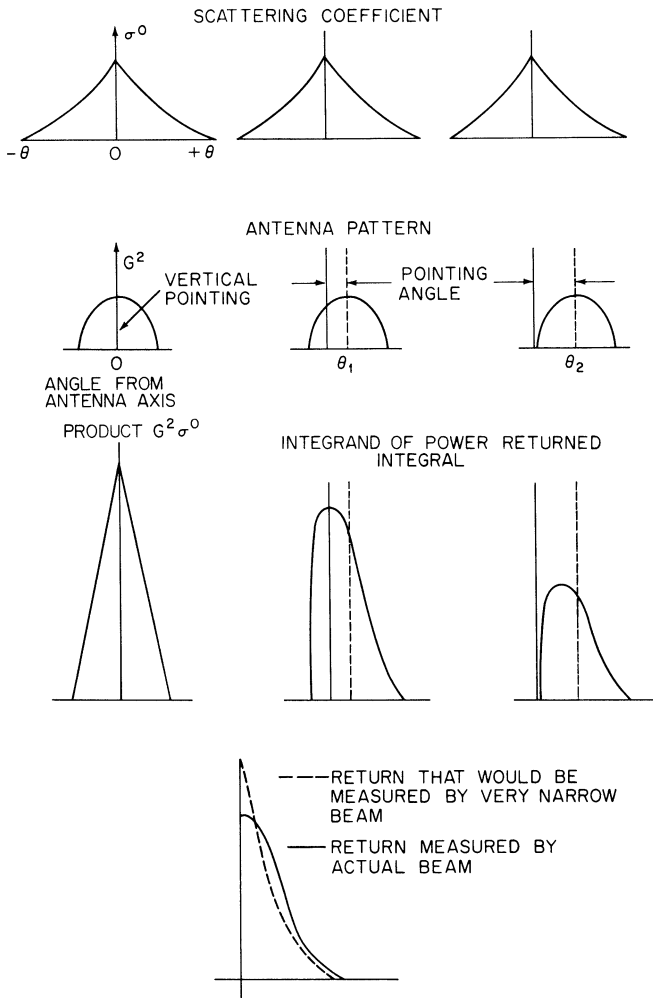


FIGURE 16.18 How finite beamwidth causes a near-vertical error in measuring the scattering coefficient

Ground and Helicopter Scatterometers and Spectrometers. Many ground scattering measurements have been made with systems mounted on boom trucks and helicopters. Most of these are FM-CW systems^{94,95} that use wide bandwidth to obtain extra independent samples rather than for fine resolution. Some use very wide bandwidth to obtain fine range resolution to locate sources of scattering.⁹⁶ Most have multiple-polarization capability, and some are capable of polarimetry because the phase of two received signals with orthogonal polarization can be measured.⁹⁷

The basic elements of an FM-CW scatterometer are shown in Figure 16.20. The swept oscillator must produce a linear sweep; this is easy with yttrium-iron-garnet (YIG)-tuned oscillators but requires linearizing circuits if tuning uses a varactor.

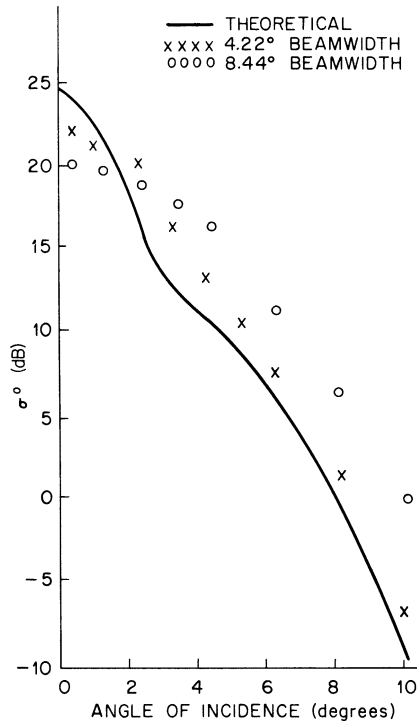


FIGURE 16.19 Effect of antenna beamwidth on the measured scattering coefficient as a function of angle of incidence

Many systems use digital waveform synthesis to obtain the swept waveform. If dual antennas are used (as shown), the overlap of the beams must be considered.⁹⁸ Single-antenna systems are sometimes used, with a circulator isolating transmitter and receiver; their performance is somewhat poorer than that of dual-antenna systems because of internal reflections and leakage through the circulator.

Figure 16.21 shows the kind of system that may be used to measure scattering from within a volume. By determining the spectrum of the return, the user can establish the scattering from different ranges. This system has been used in determining the sources of scatter in vegetation^{43–45} and snow.

Ultrasonic waves in water can be used to simulate electromagnetic waves in air.^{99–101} Because of the difference in velocity of propagation, an acoustic frequency of 1 MHz corresponds with a wavelength of 1.5 mm. Such a wavelength is of a convenient size for many modeling measurements, and, of course, equipment in the 1-MHz region is in many ways easier to operate than equipment in the microwave region; certainly it is much easier to operate and less expensive than microwave equipment operating at a 1.5-mm wavelength.

Acoustic plane waves and electromagnetic plane waves satisfy the same boundary conditions. When the scattering surfaces are not plane and when angles of incidence are rather oblique, the analogy between acoustic and electromagnetic waves is less valid. Of course, acoustic systems cannot simulate cross-polarization.

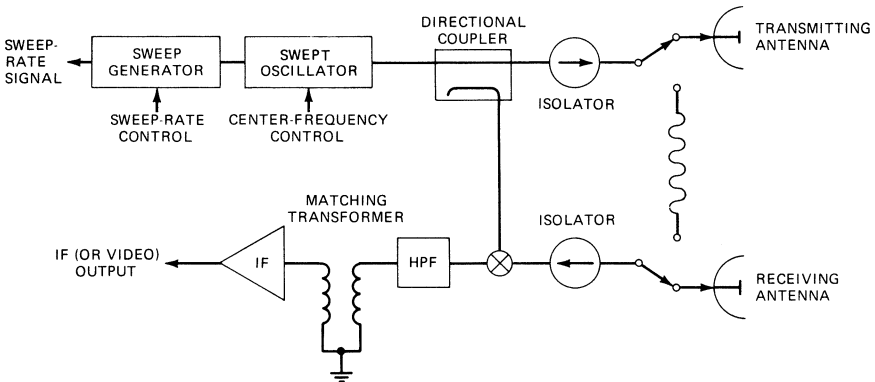


FIGURE 16.20 Basic block diagram of an FM-CW scatterometer RF section

Scattering Coefficients from Images. Radar images produced by real or synthetic aperture radars can be used for scattering coefficient measurement. Unfortunately, most such systems are uncalibrated or poorly calibrated, so the results are somewhat dubious, even on a relative basis, when images are produced on different days. Relative calibration has been introduced into some systems.^{20,28,31,102-104} Absolute calibration, which also serves as relative calibration in some cases, can be achieved by using strong reference targets, with the active radar calibrator (ARC) repeaters especially suitable.^{85,105} Another approach that has been used is to measure scattering from reference areas with a ground-based or helicopter system that is well calibrated and to compare the images to these measured values.^{102,106}

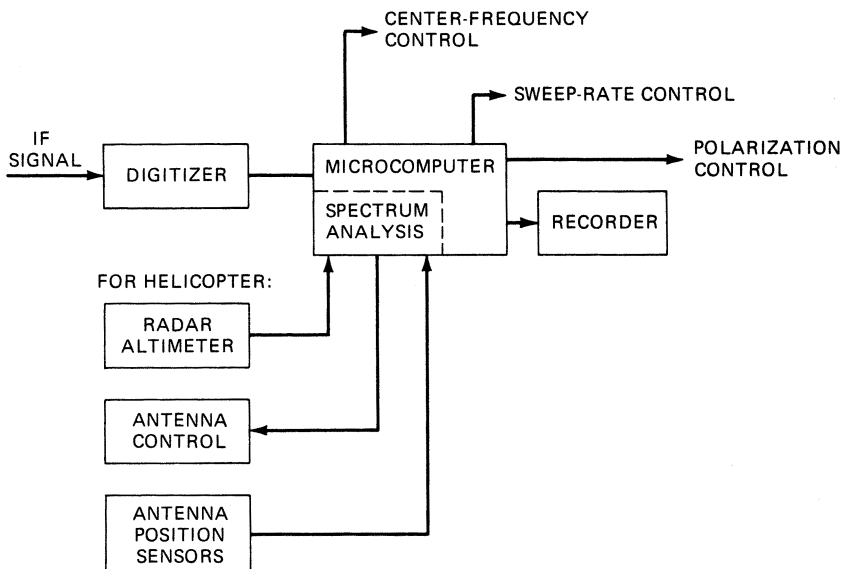


FIGURE 16.21 Basic block diagram of an FM-CW range-discriminating scatterometer: control and data-handling system

Bistatic Measurements. Measurements of ground return when the receiver and transmitter are separated are comparatively rare. These measurements are very difficult to make from aircraft because it is necessary that both transmitter and receiver antennas look at the same ground point at the same time and that the signal be correlated with known antenna look angles. Furthermore, it is difficult to know the polarization, and the exact size and shape of the common area illuminated by the antenna beams are sometimes difficult to determine. For this reason, few bistatic measurements from aircraft have been reported in the literature.¹⁰⁷

Laboratory bistatic measurements have been made by both the Waterways Experiment Station⁴² and The Ohio State University^{2,6} groups using electromagnetic waves and by the University of Kansas¹⁰⁰ group using acoustic waves. Bistatic measurements of laser radiation have been made at Bell Telephone Laboratories,¹⁰⁸ and C-band measurements of buildings have been made at the University of Kansas.¹⁰⁹ Other surface-based measurements have also been reported.^{110,111}

Bistatic measurements call for complications when made outside the laboratory because an absolute reference for both transmitter power and receiver sensitivity must be used. In the laboratory, however, it is possible to use techniques similar to those for monostatic measurements.

16.6 GENERAL MODELS FOR SCATTERING COEFFICIENT (CLUTTER MODELS)

Scatter measurements made during the 1970s allowed the generation of models for average backscatter from large areas. In particular, these included measurements with the Skylab radiometer-scatterometer RADSCAT^{83,112} and with truck-mounted microwave active spectrometers (MAS)^{112,113} by the University of Kansas. Two different models were developed based on the same data, one a linear model and one a more complicated formulation. Here we present only the linear model. These models are for *averages*, and the models do not include variations about the average. However, analysis of Shuttle Imaging Radar (SIR) data permits some estimates to be made of the variability to be expected for different sizes of illuminated footprint.

The general characteristics of radar backscatter over the range of angles of incidence have been known for decades. Figure 16.22 shows these. For like-polarized waves, one can break scatter into three angular regimes: near-vertical (the *quasi-specular region*), intermediate angles from 15 to about 80° (the *plateau region*), and near-grazing (the *shadow region*). Cross-polarized scatter does not have separate quasi-specular and plateau regions (the plateau extends to vertical), and too little is known to establish whether a shadow region exists.

For nearly every type of terrain, the measured data fits closely to the form

$$\sigma^0 = A_i e^{-\theta/\theta_i} \quad (16.23a)$$

$$\text{or} \quad \sigma_{\text{dB}}^0 = 10 \log A_i - 4.3434(\theta/\theta_i) \quad (16.23b)$$

where A_i and θ_i are constants that differ for the near-vertical and midrange regions. Figure 16.23 shows an example of this variation. No theory gives exactly this result,

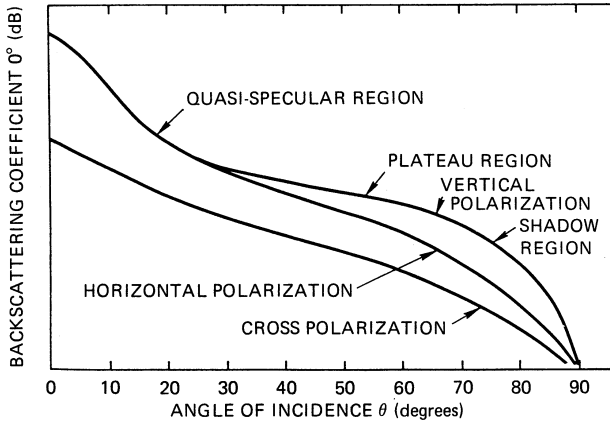


FIGURE 16.22 General characteristics of scattering coefficient variation with angle of incidence (after F. T. Ulaby, R. K. Moore, and A. K. Fung³⁷)

but nearly all measurements fit such a model closely, and the model approximates most theoretical curves well over the relevant regions. This simple result means that simple clutter models may be developed and used, although more complex models may be necessary for some remote-sensing applications.

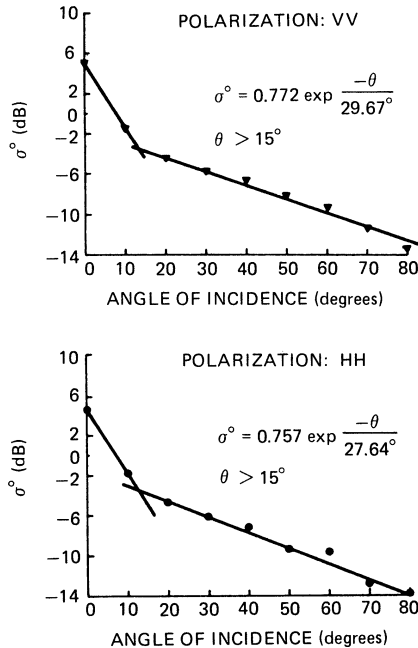


FIGURE 16.23 Regression of average of all 13.8-GHz cropland data for two years obtained with a microwave active spectrometer (after R. K. Moore, K. A. Soofi, and S. M. Purduski¹¹⁴ © IEEE 1980)

The basis for the linear model¹¹⁴ is a combination of the Skylab results over North America¹¹⁵ and those from Kansas cropland measurements over three complete seasons with the microwave active spectrometer (MAS).¹¹⁶ The 13.9-GHz Skylab RADSCAT had a ground footprint of a 10-km circle at vertical to an ellipse of 20 by 30 km at 50°. The MAS had footprints at 50° ranging from 5.5 by 8.5 m at 1.1 GHz to 1.4 by 2.1 m at 17 GHz, but millions of measurements were averaged for the model. Because the Skylab data was at only one frequency and the responses for the two experiments were essentially the same at that frequency, the frequency response shown in the model depends entirely on the MAS measurements.

The summer Skylab observations included deserts, grassland, cropland, and forests, whereas the Kansas measurements were only of cropland. However, early and late in the growing season, the cropland was essentially bare, similar to the summer desert except for soil moisture content. During the height of the growing season, the crops were dense enough so that scatter was similar to that from forests. Thus, the overall model seems representative of summer conditions averaged over all of North America.

The model takes the form

$$\sigma_{\text{dB}}^0(f, \theta) = A + B\theta + Cf + Df\theta \quad 20^\circ \leq \theta \leq 70^\circ \quad (16.24a)$$

where A , B , C , and D take on different values for different polarizations above and below 6 GHz. The frequency response below 6 GHz is much more rapid than above 6 GHz. Moreover, at frequencies above 6 GHz the frequency response is independent of angle, so that $D = 0$. For lower frequencies, the frequency response is angle-dependent.

For angles less than 20°, only two points were available, 0° and 10°, so separate frequency regressions were run at each of these angles. The model for these angles is

$$\sigma_{\text{dB}}^0(f, \theta) = M(\theta) + N(\theta)f \quad \theta = 0^\circ, 10^\circ \quad (16.24b)$$

The frequency responses below 6 GHz differed for the two years, so the models have separate values of the constants for 1975 and 1976. The year 1976 was very dry in Kansas: therefore, the 1975 values are probably more representative, but both are given here. Values of the constants are in Table 16.2. Figure 16.24 shows the clutter model for the midrange of angles as a function of frequency.

TABLE 16.2 Constants for Linear Scattering Model (Summer)*

Eq.	Polarization	Angular Range, °	Frequency Range, GHz	Constant A or M , dB	Angle Slope B or N , dB	Frequency Slope C , dB/GHz	Slope Correction D , dB/(° × GHz)
16.24a	V	20–60	1–6 (1975)	−14.3	−0.16	1.12	0.0051
	V	20–50	1–6 (1976)	−4.0	−0.35	−0.60	0.036
	V	20–70	6–17	−9.5	−0.13	0.32	0.015
	H	20–60	1–6 (1975)	−15.0	−0.21	1.24	0.040
	H	20–50	1–6 (1976)	−1.4	−0.36	−1.03	
	H	20–70	6–17	−9.1	−0.12	0.25	
16.24b	V and H	0	1–6 (1975)	7.6	...	−1.03	
	V and H	0	1–6 (1976)	6.4	...	−0.73	
	V and H	0	6–17	0.9	...	0.10	
	V and H	10	1–6 (1975)	−9.1	...	0.51	
	V and H	10	1–6 (1976)	−3.6	...	−0.41	
	V and H	10	6–17	−6.5	...	0.07	

* After R. K. Moore, K. A. Soofi, and S. M. Purduski¹¹⁴ © IEEE 1980

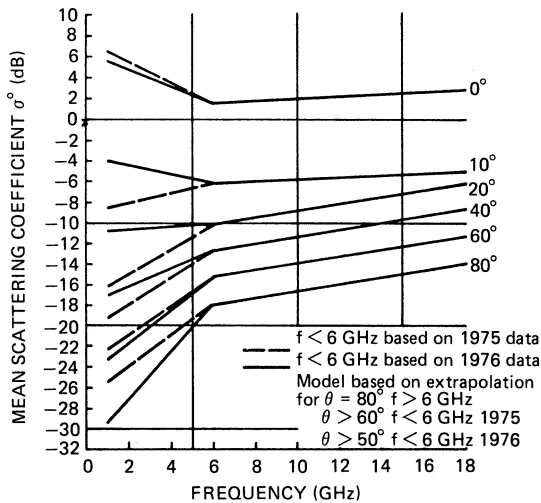


FIGURE 16.24 General land-scattering-clutter model (vertical polarization). Horizontal polarization is very similar. (after R. K. Moore, K. A. Soofi, and S. M. Purduski¹¹⁴ © IEEE 1980)

The figure is only for vertical polarization because results are so similar for vertical and horizontal.

Ulaby developed a different, more complex model from the Kansas vegetation data.¹¹⁷ This model fits curves rather than straight lines to the measured data. For most purposes, the straight-line model is adequate, and it is much easier to use.

A straight-line model for snow-covered grassland similar to that for vegetation depends on a more limited data set.^{118,119} The data was for only one season in Colorado when the snow was only about 50 cm deep. This means that the signal probably penetrated to the ground surface at frequencies below about 6 GHz. Nevertheless, the model indicates the kind of results to be expected for this important situation. Table 16.3 gives the resulting constants to use in Eq. 16.24a.

TABLE 16.3 Regression Results for Ground-Based Measurements of Snow-Covered Ground*

Time of Day	Polarization	Frequency Range, GHz	Constant A, dB	Angle Slope B, dB/°	Frequency Slope C, dB/GHz	Slope Correction D, dB/(° × GHz)
Day	V	1–8	–10.0	–0.29	0.052	0.022
Day	V	13–17	0.02	–0.37	–0.50	0.021
Day	H	1–8	–11.9	–0.25	0.55	0.012
Day	H	13–17	–6.6	–0.31	0.0011	0.013
Night	V	1–8	–10.0	–0.33	–0.32	0.033
Night	V	13–17	–10.9	–0.13	0.70	0.00050
Night	H	1–8	–10.5	–0.30	0.20	0.027
Night	H	13–17	–16.9	–0.024	1.036	–0.0069

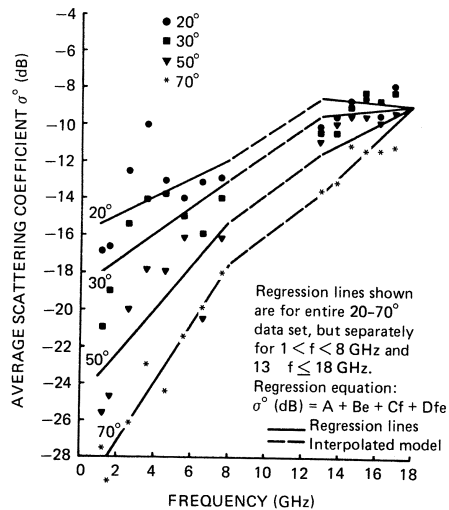
* After R. K. Moore, K. A. Soofi, and S. M. Purduski¹¹⁴ © IEEE 1980

NOTE: $\theta = 20$ to 70° . Values of coefficients in this table are also considered those of the model.

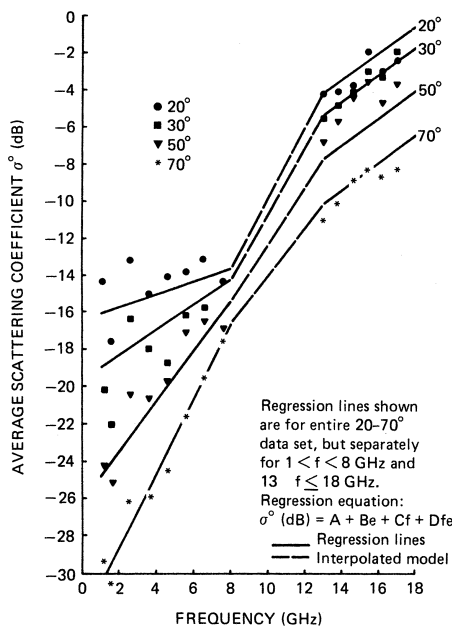
Snow scatter depends strongly on the free-water content of the upper layer of snow, so scatter is much lower from the wet daytime snow (where solar melting has commenced) than for the dry nighttime snow. Hence, different models must be used for day and night; compare the day and night measurements shown in Figure 16.25. The difference between day and night scatter from snow is even more pronounced at 35 GHz, but the model does not include 35 GHz because no data exists between 17 and 35 GHz.

Although no specific clutter model has been developed for forests, results from the Skylab RADSCAT and Seasat scatterometer show that the Amazon rainforest scatters almost independently of the angle of incidence even near vertical.¹²⁰ The mean measured value at 33° was -5.9 ± 0.2 dB at 13.9 GHz. Similar results were found at C band.¹²¹ Observations with SIR-B, SIR-C, and JERS-1 indicated that this lack of angular variation of σ^0 also is present at 1.25 GHz.^{122,123}

The models described above are based on averages over very large areas. For this situation, the variability from place to place is small, particularly in the midrange of angles. Figure 16.26 shows the mean and upper and lower decile values measured by the Skylab RADSCAT over North America. The large variation near vertical apparently results from the effect of nearly specular reflection from water bodies. When the footprint is smaller, more variability occurs. This is shown in Figure 16.27 from a study of the variation of scatter observed by SIR-B with averages over different-sized footprints. For small footprints, the scatter varies over a wide range, and system designers must account for this.



(a)



(b)

FIGURE 16.25 Regressions for vertical-polarization clutter model for snow: (a) day and (b) night. Note the large differences. Horizontal polarization is similar. (after R. K. Moore, K. A. Soofi, and S. M. Purduski¹¹⁴ © IEEE 1980)

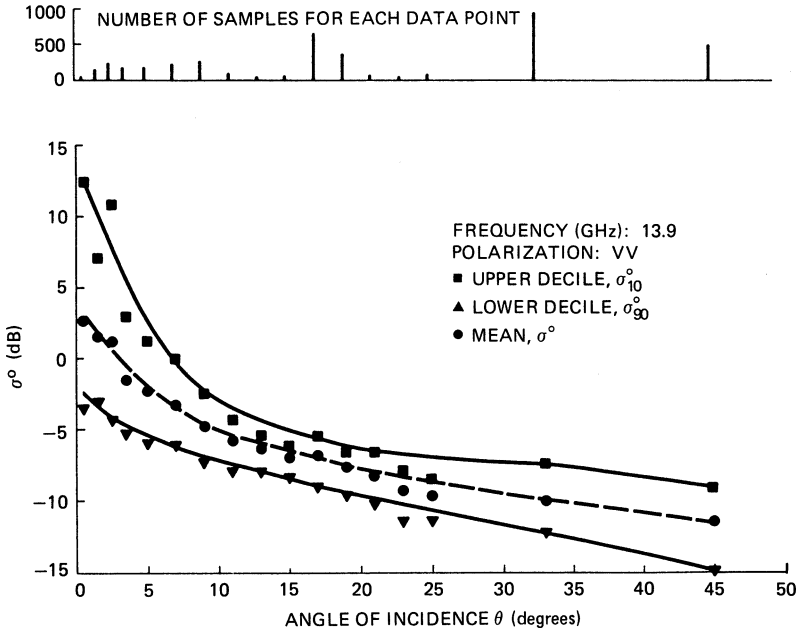


FIGURE 16.26 Angular patterns of the mean, upper decile, and lower decile of Skylab scatterometer observations over North America during the summer season (from Moore *et al.*, University of Kansas Remote Sensing Laboratory Technical Report 243-12, 1975)

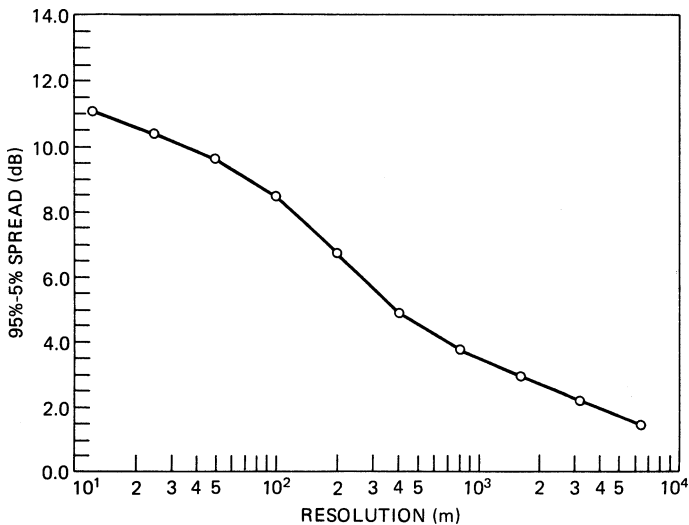


FIGURE 16.27 90% range of pixel amplitude versus resolution

16.7 SCATTERING COEFFICIENT DATA

Numerous programs to gather scattering coefficient data existed prior to 1972, but sizable data collections with accompanying “ground truth” were rare. Since 1972, however, several major programs have changed the situation so that much information is now available. Indeed, this information is so widespread that an adequate summary of the literature is impossible. Hence, this section can only give highlights of the results and major programs. The reader should consult the three major compendia of such data for more information both on results and on bibliography^{37,38,40} (note that information is spread through many chapters of these volumes).

Some early scattering-coefficient-measurement programs worth mentioning include those of the Naval Research Laboratory,^{23,24} Goodyear Aerospace Corporation,²⁰ Sandia Corporation (near-vertical data),^{124,125} and particularly The Ohio State University.^{2,6} From 1972 to 1984, the largest program was at the University of Kansas.^{8,9,37,72,83,98,126} Extensive programs were also in France (Centre National d’Etudes Spatiales, Centre National d’Etudes des Télécommunications, Université Paul Sabatier),^{12,127} the Netherlands,^{10,128} Canada Centre for Remote Sensing (CCRS; especially sea ice),^{26,129} and Switzerland and Austria (snow).^{130,131} Many of the results from these programs appear in digests of the International Geoscience and Remote Sensing Symposia (IGARSS; IEEE Geoscience and Remote Sensing Society) and journals such as *IEEE Transactions on Geoscience and Remote Sensing* and on *Ocean Engineering*, *International Journal of Remote Sensing*, *Remote Sensing of Environment*, and *Photogrammetric Engineering and Remote Sensing*.

Although calibrations for some of the older data were doubtful, summary presentations are not available for newer data. Accordingly, Figure 16.28 shows an earlier summary based mostly on X-band data. One should be cautious in using this data, but the figure gives a feel for the overall variations. Figure 16.29 is a similar presentation for near-vertical data.¹³² Calibration of the systems was good, but the antenna effect discussed in Section 16.5 makes the values from 0 to 5° low.

Effects of Roughness, Moisture Content, and Vegetation Cover. Scattering falls off more rapidly with angles for smooth surfaces than for rough surfaces. Since the roughness that affects radar must be measured in wavelength units, a surface smooth at long wavelengths may be rough at shorter ones. This is illustrated in Figure 16.30,¹³³ which shows these effects with measurements from plowed fields. At 1.1 GHz, the signal changed 44 dB between 0 and 30° for the smoothest field and only 4 dB for the roughest. At 7.25 GHz the smoothest field was rough enough to reduce the variation to 18 dB.

For most surfaces, cross-polarized scatter is lower than like-polarized scatter, often by about 10 dB. Cross-polarized scatter from smooth surfaces is much less near vertical than elsewhere. Figure 16.31¹³⁴ shows this effect. Cross-polarized returns from volume scatterers with elements that are large compared with a wavelength are stronger than for surfaces, sometimes being only 3 dB down.

Scatter depends on the dielectric constant, which depends on moisture content. Thus, scatter from wet soils at angles off vertical is usually much higher than from dry soils. Figure 16.32 shows this.¹² The effect can be many decibels (9 dB in the figure).

Vegetation canopies over soil can contribute to scatter in the various ways shown in Figure 16.33.¹³⁵ Figure 16.34⁴³ shows an example. Most of the scatter from the entire plant came from the top leaves, with enough attenuation there to reduce

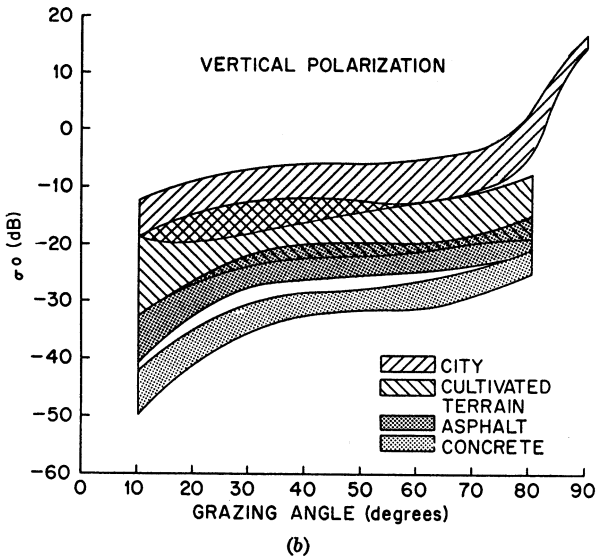
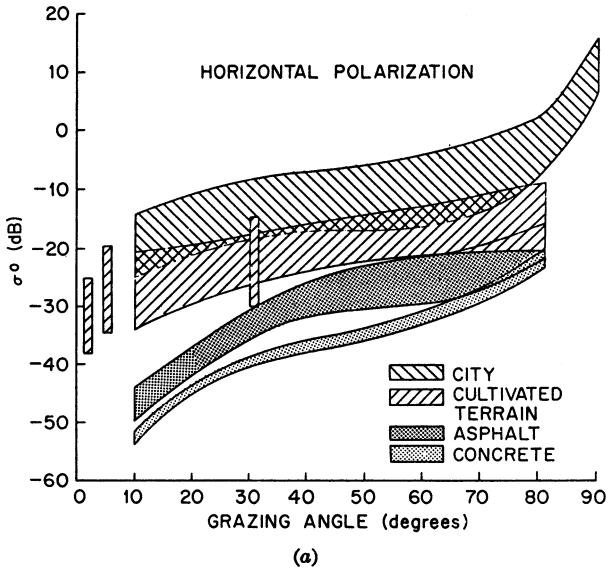


FIGURE 16.28 Boundaries of measured radar data: (a) horizontal polarization and (b) vertical polarization (Courtesy of I. Katz)

the scatter from stem, bottom leaves, and soil to measurable but negligible size. When those leaves were absent, the signals scattered from the soil and lower parts of the plant were about equal to each other and were much larger than when leaves were present.

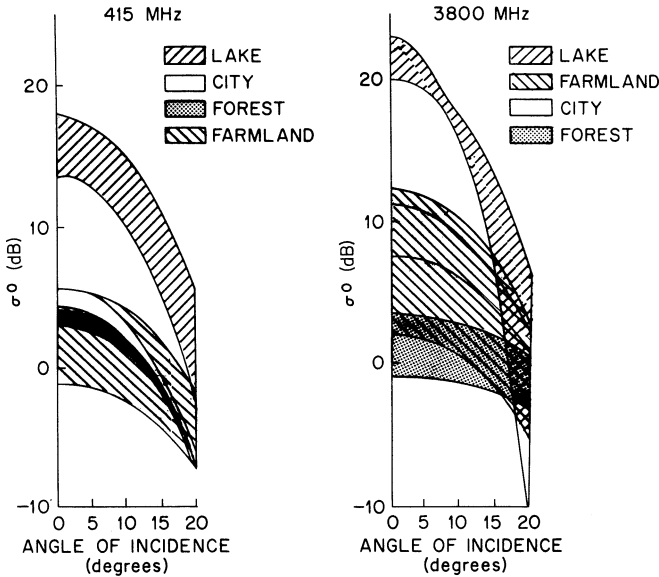


FIGURE 16.29 Boundaries of measured radar return near vertical incidence, based on Sandia Corporation data (from F. J. Janza, R. K. Moore, and B. D. Warner¹³²)

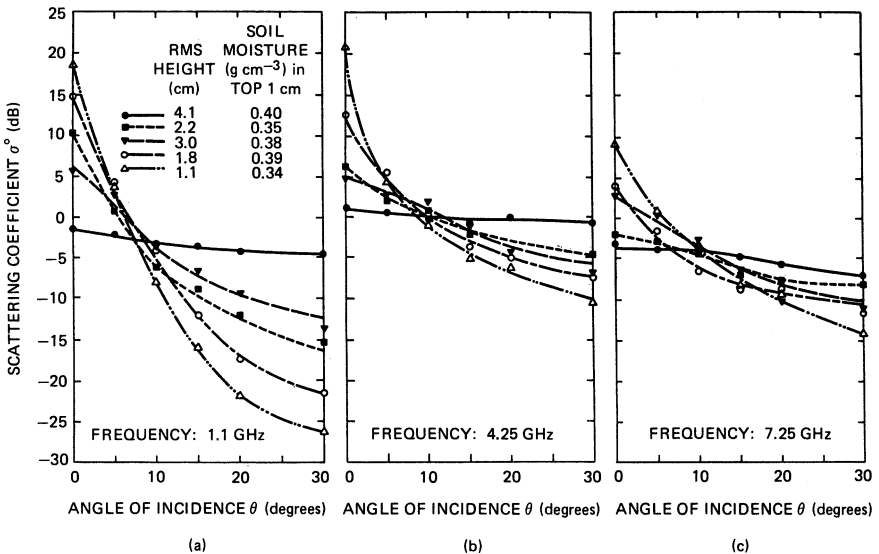


FIGURE 16.30 Angular response of the scattering coefficient for five moist fields with different roughness at (a) 1.1 GHz, (b) 4.25 GHz, and (c) 7.25 GHz (after F. T. Ulaby, R. K. Moore, and A. K. Fung³⁷)

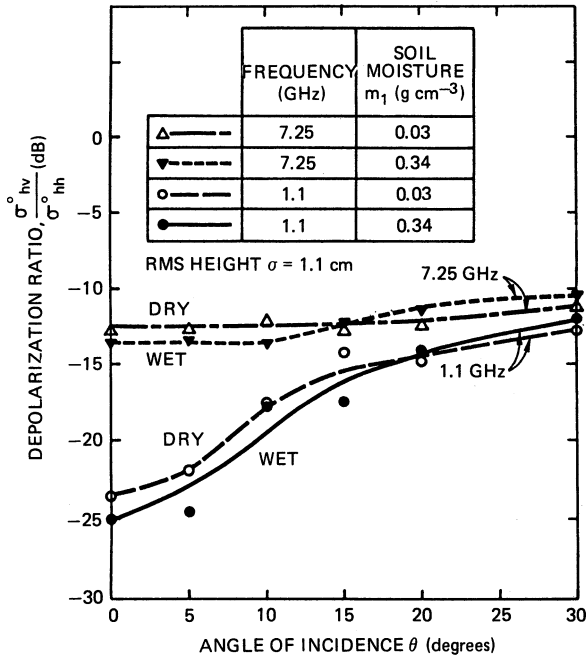


FIGURE 16.31 Angular dependence of the depolarization ratio of a smooth surface (after F. T. Ulaby, R. K. Moore, and A. K. Fung³⁷)

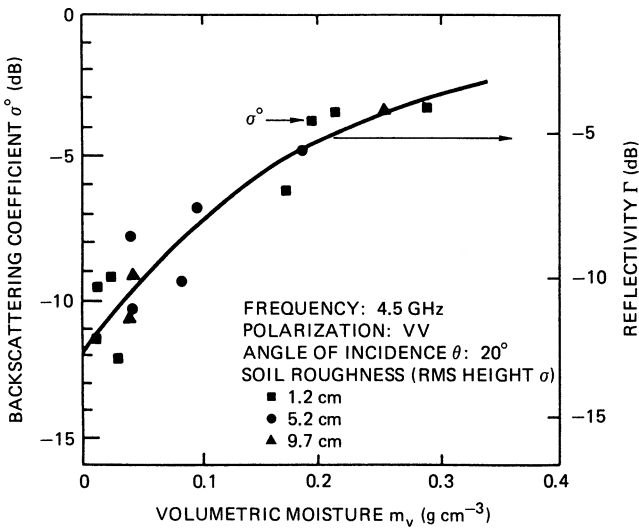


FIGURE 16.32 Measured scattering coefficient σ^o (left scale) as a function of soil moisture content for three surface roughnesses. The solid curve is the reflectivity Γ (right scale) calculated on the basis of dielectric measurements. (after T. LeToan¹² © IEEE 1982)

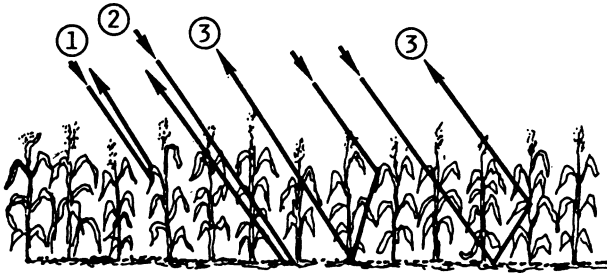


FIGURE 16.33 Contributions to backscatter from a vegetation canopy over a soil surface: (1) direct backscattering from plants, (2) direct backscattering from soil (includes two-way attenuation by canopy), and (3) plant-soil multiple scattering (after F. T. Ulaby, R. K. Moore, and A. K. Fung³⁷)

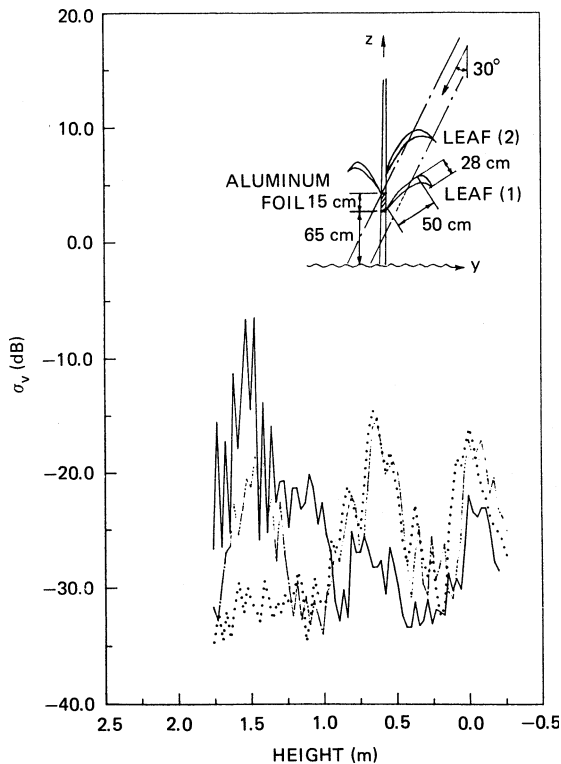


FIGURE 16.34 FM-CW probing scatterometer measurements of a corn plant at 30°. The solid curve is the full plant; the dot-dash curve, leaf 1 removed; the dotted curve, leaf 2 removed. (after L. K. Wu *et al.*⁴³)

Because volume scatter dominates for dense vegetation, especially trees, σ^0 is nearly independent of the angle of incidence. Figure 16.35¹³⁶ shows this with results from X-band imaging of a forest. The figure is a plot of γ rather than σ^0 ($\gamma = \sigma^0 / \cos \theta$). At low frequencies such as VHF, this condition changes because the attenuation through the leaves and branches is less.¹³⁷

Soil Moisture. Figure 16.32 shows the size of the effect of soil moisture on σ^0 . Soil moisture effects differ for different soils. Dobson and Ulaby¹³⁸ showed that this use of moisture expressed in percent of *field capacity* improved the fit between σ^0 and moisture content. Field capacity is a measure of how tightly the soil particles bind the water; the unbound water affects ϵ more. An empirical expression for field capacity (FC) is¹³⁹

$$FC = 25.1 - 0.21S + 0.22C \text{ percent by weight}$$

where S and C are the percentages (by weight) of sand and clay in the soil. The soil moisture content in terms of field capacity is

$$m_f = 100m_g / FC \text{ percent}$$

with m_g the percent moisture in the soil by weight. When we use this measure, the relation between σ^0 in dB and m_f is linear even in the presence of moderate vegetation cover, as shown in Figure 16.36¹⁴⁰. The slope of this curve is somewhat different with vegetation cover than it is without, however. Although m_f is apparently at least as good as the volumetric moisture content for relating to σ^0 , its use has been questioned.¹⁴¹

Soil moisture can affect a radar image, as has been demonstrated in imagery obtained from the Seasat L-band SAR.¹⁴² A simulation experiment¹⁴³ showed that one can estimate soil moisture within 20% for 90% of the pixels in an image. Moreover, it showed that resolutions between 100 and 1000 m were superior to finer resolutions

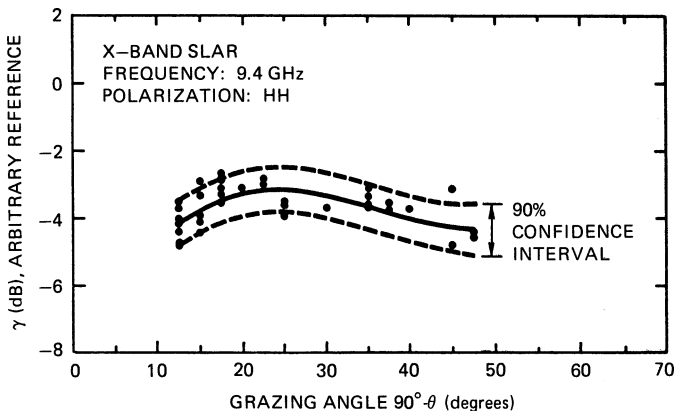


FIGURE 16.35 Measured scattering variation of a forest parcel of old beech trees. Note use of γ (with an arbitrary reference) instead of σ^0 for the ordinate. (after D. H. Hoekman¹³⁶)

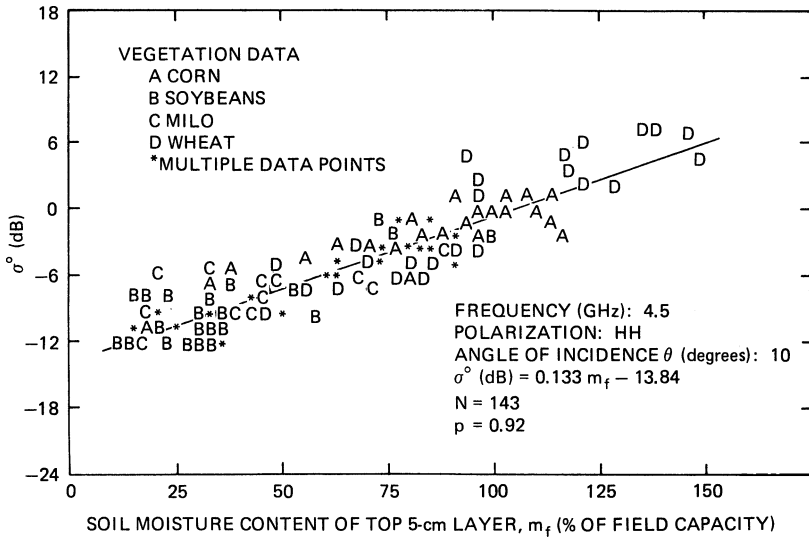


FIGURE 16.36 4.5-GHz scattering coefficient versus soil moisture (percent of field capacity) for vegetation-covered soil (after F. T. Ulaby *et al.*¹⁴⁰)

for this purpose. Most of the spaceborne SARs that followed Seasat have been used in soil-moisture studies.^{144,145,146}

Vegetation. Backscatter from vegetation depends on many parameters and varies widely. Thus, although we can develop *average* models like those described in Section 16.6, details are much more complex. The σ^0 varies with season, moisture content, state of growth, and time of day.

Figure 16.37¹⁴⁷ shows the seasonal variation for corn compared with a model presented in the reference. The much larger variation at σ^0 apparently results from the larger effect at vertical of the soil and consequently its moisture content. The rapid 12 dB swing between May 25 and June 1 results from drying of the soil. Even at 50°, where attenuation through the canopy masks the soil effect, the seasonal variation exceeds 8 dB. Diurnal variations are relatively small but finite. They result both from plant moisture changes and from morphological changes (a corn plant actually lifts its leaves “to meet the sun”; morning glories close their flowers at night).

Most crops are planted in rows. This causes an azimuthal variation of σ^0 , as shown in Figure 16.38.¹⁴⁸ The modulation shown is the ratio of σ^0 looking parallel to the rows (more vegetation) to that looking normal. This phenomenon is much more pronounced at the lower frequencies.

Some general properties of vegetation scatter are visible in Figure 16.39.¹⁴⁹ At low frequencies, the decay with θ is rapid out to about 20° and then more gradual; most of the steep part results from surface echo. At higher frequencies, the plant attenuation prevents a significant surface echo, so the angular variation is more uniform.

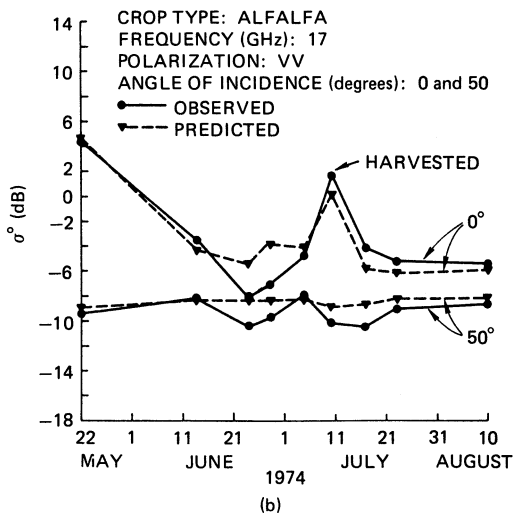
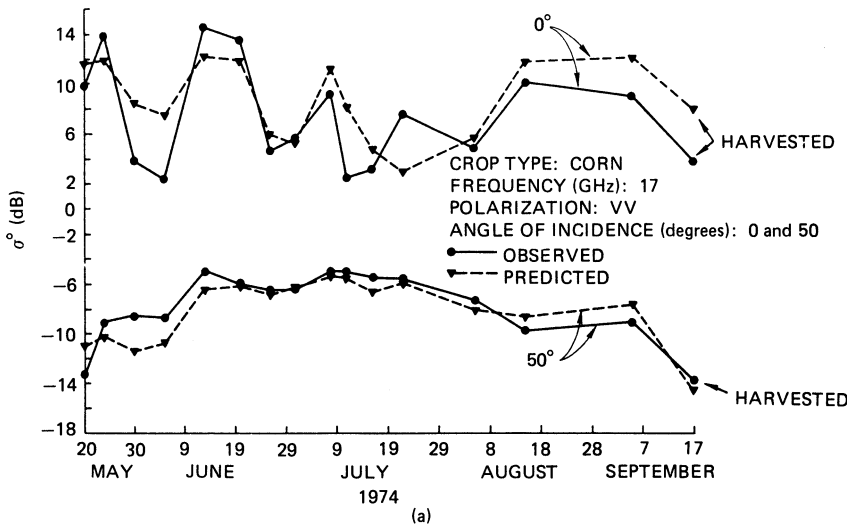


FIGURE 16.37 Time variation of scatter from (a) corn and (b) alfalfa at incidence angles of vertical and 50° (after E. Attema and F. T. Ulaby¹⁴⁷)

Cross-polarized signals at vertical are negligible, so even at low frequencies, the cross-polarized σ^0 varies uniformly. At both high and low frequencies, it is about 10 dB below the like-polarized σ^0 .

Snow. When snow covers the ground, much of the scatter is from the snow rather than the underlying ground. Snow is both a volume-scattering and an attenuating medium. When the snow is dry, scatter comes from a large volume; when it is wet, the scattering volume is much less because of higher attenuation. As a result,

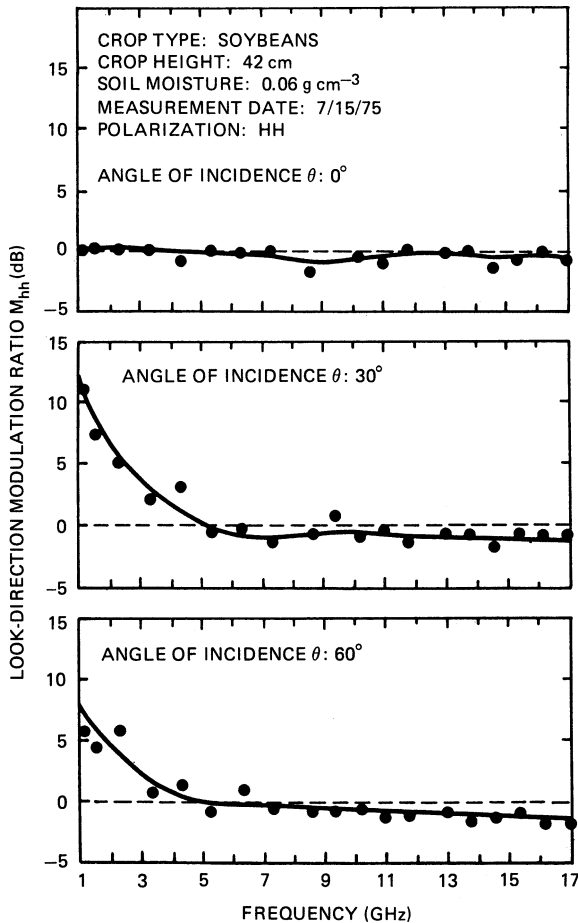


FIGURE 16.38 Frequency response of the look-direction modulation ratio for a soybean field with horizontal polarization at incidence angles of 0, 30, and 60° (after F. T. Ulaby, R. K. Moore, and A. K. Fung³⁷)

σ^0 decreases rapidly as the sun melts the top layer. Figure 16.40¹⁵⁰ illustrates how fast this can be and also shows that the effect is much greater at the higher frequencies where attenuation is greater. Figure 16.41¹⁵¹ shows the angular variation seen for snow-covered ground. Off-vertical scattering is much greater at higher frequencies. For the 58-cm depth shown, much of the scatter at 1.6 and 2.5 GHz is probably from the underlying surface.

Some reports state that there are *radar hot spots* in snow cover, particularly at 35 GHz. These reports result from improper interpretation of variations that are due to normal Rayleigh fading of the signal. Scatter from snow comes from many centers within the illuminated volume, so the conditions for Rayleigh fading are met.

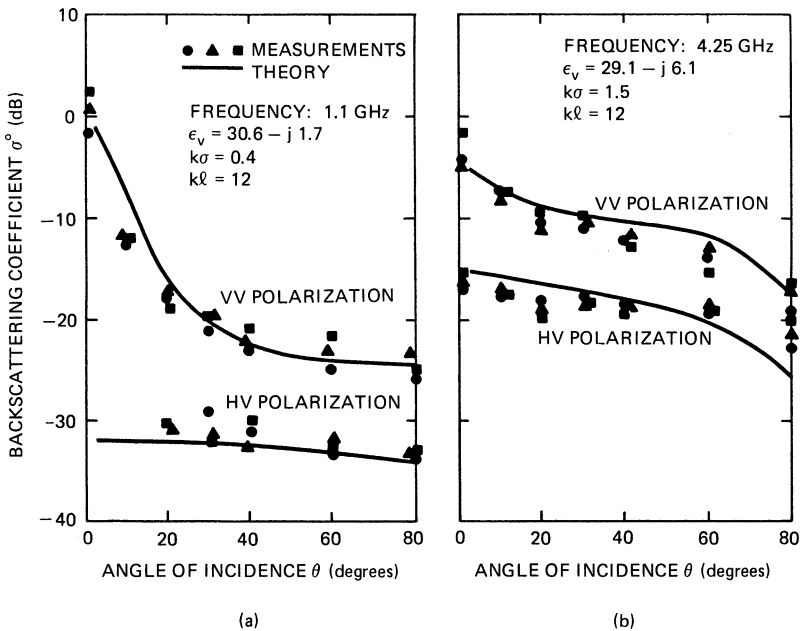


FIGURE 16.39 Comparison of model calculations with measurements at (a) 1.1 GHz and (b) 4.25 GHz (after H. Eom and A. K. Fung¹⁴⁹)

Measurements with suitable averaging in frequency or illumination angle demonstrate that snow-covered surfaces scatter essentially uniformly except for the effects of the multipath fading.

Sea Ice. Sea ice is a very complex medium. Ice observers characterize it in many different categories that depend on thickness, age, and history of formation.¹⁵² Hence, one cannot characterize its radar return in any simple way; in this sense, it is like vegetation. The most important ice types from a radar point of view are first-year (FY 1 to 2 m thick), multiyear (MY > 2 m thick), and a conglomeration of thinner types (< 1 m thick).

Like snow, sea ice influenced by solar melting and above freezing temperatures scatters microwaves very differently from the more normal cold-surface ice. In winter, the cold MY ice scatters much more than cold FY ice. In summer, σ^0 for MY ice decreases to about the same level as that of FY ice. Figure 16.42¹⁵³ shows this and typical angular responses. These curves are for 13.3 GHz, but the results would be similar at any frequency down to S band. Figure 16.43¹²⁶ shows the frequency variation of σ^0 for various kinds of ice. Shore-fast ice is grounded to the bottom at the shoreline; in this case, it is probably MY. Gray ice is one of the types thinner than FY.

Kim⁷² developed a theory that explains a wide range of sea-ice σ^0 measurements. From this and extensive data from the literature on ice properties, Figure 16.44⁹¹ shows the ranges of FY and MY scattering under winter conditions. Clearly higher frequencies are better for identifying ice types than lower frequencies, and

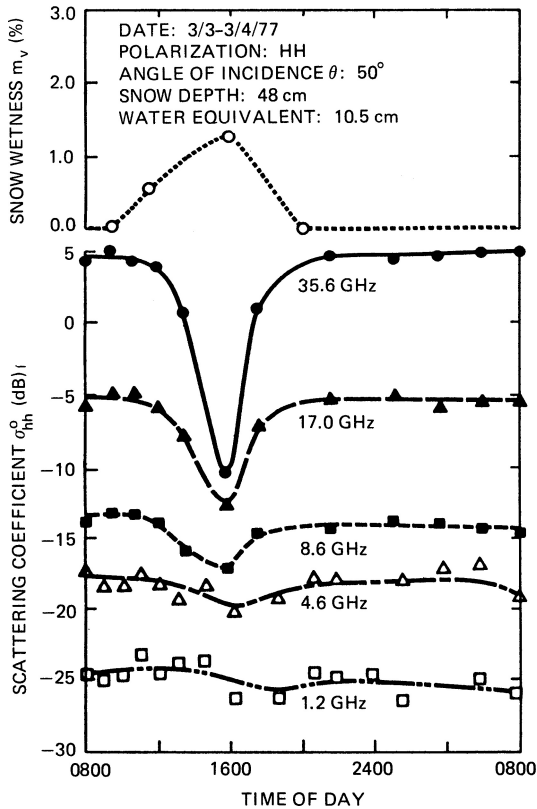


FIGURE 16.40 Diurnal patterns of σ^0 and liquid-water content for snow at several frequencies. Note the extreme variation of the K_u band as the sun starts to melt the surface. (after W. H. Stiles and F. T. Ulaby¹⁵⁰)

discrimination is not possible below about 5 GHz. At L band and below, the differences between MY and FY ice are small even in winter. This means that imaging radars can easily distinguish ice types by intensity alone at the higher frequencies in winter but not in summer. This fact is the basis for operational ice-monitoring systems by the Soviet Union [using the Toros K_u -band side-looking airborne radar (SLAR)]¹⁵⁴ and Canada¹⁵⁵ (using a modified X-band APS-94 SLAR and the STAR-1 X-band SAR). A prime motivation for the Canadian Radarsat SAR was monitoring of sea ice, which the system has been doing successfully since 1995.^{156,157} The Russian X-band real-aperture radars in the Okean series have been used for similar purposes.^{158–160}

Snow cover on ice can mask ice scatter itself as with snow on land. Since the arctic is relatively dry, most areas have little snow, but snow does make distinguishing ice types difficult at times. This is particularly true in the Antarctic, where snow is more prevalent on the sea ice.¹⁶¹

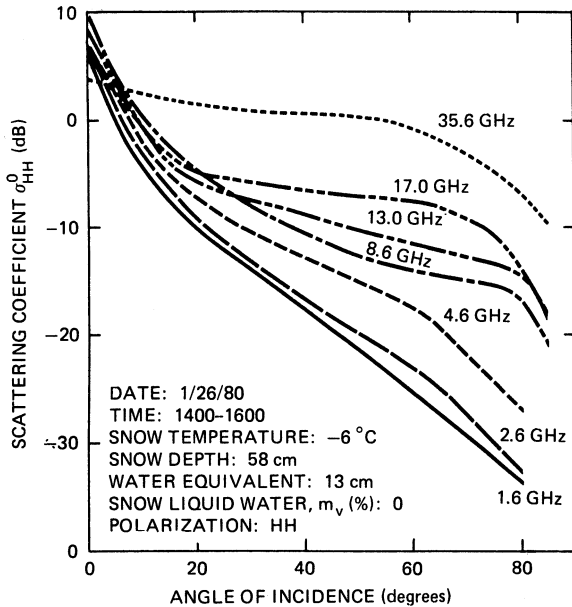


FIGURE 16.41 Angular response of σ^0 of dry snow at different frequencies. Rapid falloff at lower frequencies apparently results from penetration to the smooth ground surface. (after W. H. Stiles *et al.*¹⁵¹)

Programs to learn microwave properties of sea ice have been numerous because of the importance of arctic operations and meteorology. Microwave remote sensing is necessary to monitor ice properties in the arctic owing to the long winter night, frequent cloud cover, and inaccessibility.

16.8 POLARIMETRY

Several synthetic-aperture imaging radars are capable of measuring the full complex polarization matrix. Probably the first of these was an airborne system built by NASA's Jet Propulsion Laboratory. The first one in space was the Shuttle Imaging Radar-C (SIR-C). Although use of multiple polarizations dates from the early days of imaging radars, the measurement of phase between the received signal with different polarizations is more recent, dating from the late 1980s. Few, if any, full-polarimetric data sets exist of the type described above for single polarizations. For more complete discussions of radar polarimetry, consult references Ulaby and Elachi,¹⁶² Sletten and McLaughlin,¹⁶³ and van Zyl and Kim.¹⁶⁴

Since polarimetric radars use defined phases for both transmit and receive, the signals must be described in the form used for elliptical polarization. This is illustrated in Figure 16.45.

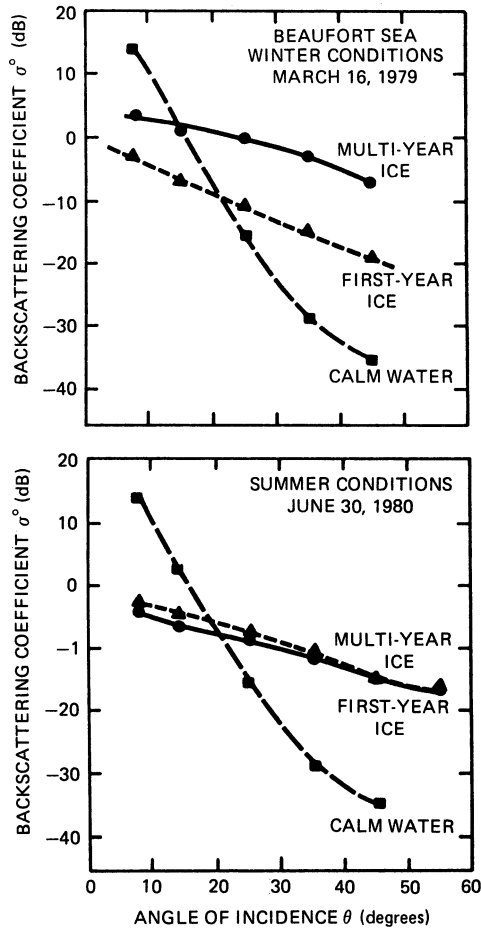


FIGURE 16.42 Comparison of sea-ice scattering at 13.9 GHz in summer and winter (after A. L. Gray *et al.*¹⁵³ © IEEE 1982)

When $\chi = 0$, the polarization is linear with the E vector in the direction given by ψ . When $\chi = \pm 45^\circ$, the polarization is circular, with $+45^\circ$ for left-hand and -45° for right-hand. When $0 < |\chi| < 45^\circ$, the polarization is elliptical.

Analytically, the electric field may be described as

$$\mathbf{E} = E_h \mathbf{1}_h + E_v \mathbf{1}_v \quad (16.25)$$

where $\mathbf{1}_h$ and $\mathbf{1}_v$ are unit vectors in the h and v directions. The instantaneous fields are given by Eq. 16.26, where the δ_s show the different phases for the components of \mathbf{E} and k is the wavenumber.

$$e_h(t) = \text{Re } E_h e^{j(\omega t - kx + \delta_h)} \quad (16.26a)$$

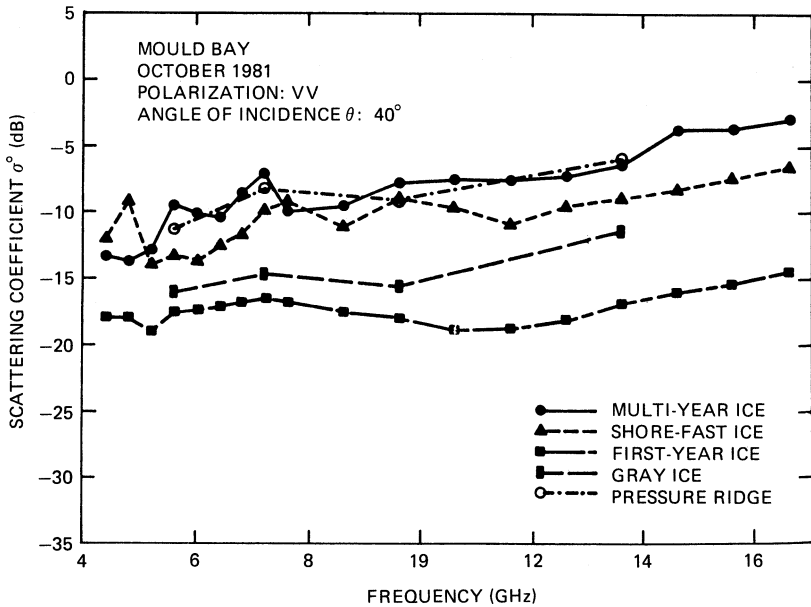


FIGURE 16.43 Example of frequency response of σ^0 for different kinds of sea ice (from Y. S. Kim⁷²)

and

$$e_v(t) = \text{Re } E_v^{j(\omega t - kz + \delta_v)} \quad (16.26b)$$

In complex format

$$E_h = E_{h0} e^{j\delta_h} \quad \text{and} \quad E_v = E_{v0} e^{j\delta_v}$$

If we take $\delta = \delta_v - \delta_h$ and set $\delta_v = 0$ as a reference, we can write

$$E = E_{h0} e^{-j\delta} + E_{v0} 1_v$$

Thus, for a single wave, we need only have three independent parameters. In radar, we must consider both transmitted and received polarimetric signals, so the need for four magnitudes and two phases.

Another way to describe polarimetric signals is to use the matrix of Stokes parameters:

$$\mathbf{F} = \begin{bmatrix} I_0 \\ Q \\ U \\ V \end{bmatrix} = \begin{bmatrix} |E_h|^2 + |E_v|^2 \\ |E_h|^2 - |E_v|^2 \\ 2\text{Re}(E_h E_v^*) \\ 2\text{Im}(E_h E_v^*) \end{bmatrix} \quad (16.27)$$

The individual Stokes parameters I_0 , Q , U , and V are defined as shown in Eq. 16.27.

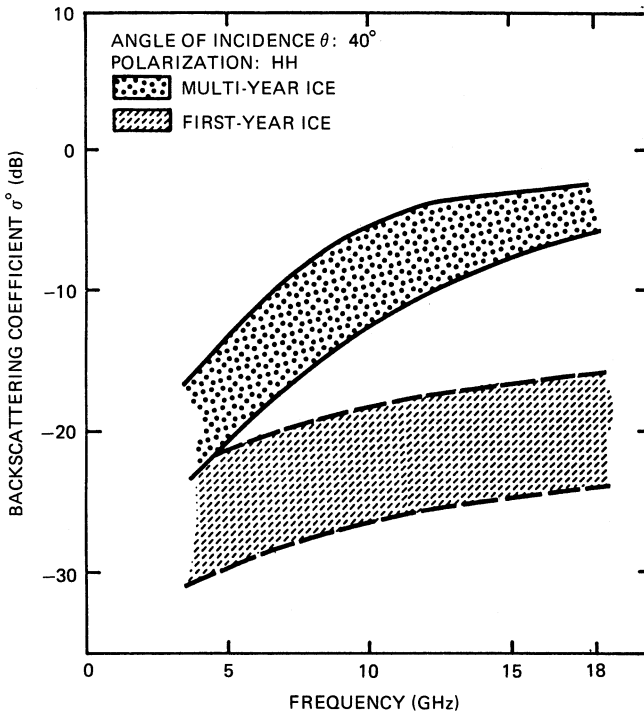


FIGURE 16.44 Measurement-based theoretical σ^0 variations for first-year and multiyear sea ice. Ranges are determined by using known variations of ice characteristics. (after Y. S. Kim *et al.*¹²⁶)

Some of the return signals from a resolution cell maintain their polarization characteristics over time and space, whereas others have a random polarization. This occurs, as for sunlight, when the polarization ellipse changes its properties randomly and rapidly with time or with small differences in angle. When both the persistent and random parts

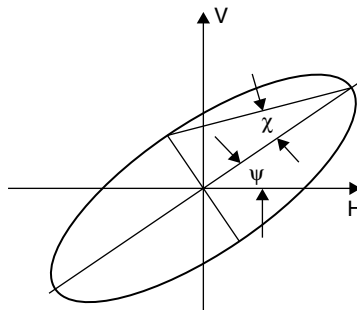


FIGURE 16.45 Polarimetric ellipse: χ is the ellipticity angle, and ψ is the orientation angle. The ellipse is the locus of the end of the E vector throughout a cycle.

are present, the target is said to be partially polarized; when no random component is present, the target is fully polarized. Radar signals are frequently only partially polarized, especially where multiple bounces occur within the target area.

For the nonrandom part, we must define a Stokes vector using an ensemble average of each component; the averaging may be over time or look angle. Thus we have

$$\mathbf{F} = \begin{bmatrix} \langle |E_h|^2 + |E_v|^2 \rangle \\ \langle |E_h|^2 - |E_v|^2 \rangle \\ \langle 2\text{Re}(E_h E_v) \rangle \\ \langle 2\text{Im}(E_h E_v) \rangle \end{bmatrix} \quad (16.28)$$

when the wave is completely polarized,

$$I_0^2 = Q^2 + U^2 + V^2 \quad (16.29)$$

but when it is partially polarized,

$$I_0^2 > Q^2 + U^2 + V^2 \quad (16.30)$$

In fact, when the wave is completely unpolarized (sunlight, for example), E_v and E_h are uncorrelated, so U and V are both zero.

Waves of this type are used in polarimetric radar; however, to see how the scattering coefficient works, we need to consider both the incident and scattered wave.

At this point, we must introduce the scattering matrix \bar{S} . The received field may be represented by

$$\mathbf{E}^r = \frac{e^{-jkR}}{R} \bar{S} \mathbf{E}^i \quad (16.31)$$

where

$$\mathbf{E}^r = \begin{bmatrix} E_v^r \\ E_h^r \end{bmatrix} \quad \text{and} \quad \mathbf{E}^i = \begin{bmatrix} E_v^i \\ E_h^i \end{bmatrix}$$

and

$$\bar{S} = \begin{bmatrix} S_{vv} & S_{vh} \\ S_{hv} & S_{hh} \end{bmatrix} \quad (16.32)$$

In the usual reciprocal media, $S_{vh} = S_{hv}$. Since the choice of a phase reference is arbitrary, there are then three independent magnitudes ($|S_{vv}|$, $|S_{hh}|$, $|S_{hv}|$), but only two independent phases ($\angle S_{hh}$, $\angle S_{hv}$). These quantities can be used to describe the properties of the polarized part of the echo from a target.

We can also describe the scattering using the Mueller matrix that is related to the Stokes matrix. The reader is referred to the literature for further descriptions of the Mueller matrix.^{162,165}

The usual way to obtain polarized responses is to transmit alternate vertically and horizontally polarized pulses. Presuming there is almost no change in the target during the interpulse interval, the responses may be combined to produce the scattering matrix or Mueller matrix. By combining the signals in processing, this method permits synthesizing *equivalent transmitted polarizations* with any ellipticity and orientation.

A commonly used way to describe the polarization characteristics of a target is the *polarization signature*.³² This consists of two three-dimensional graphs. For the first graph, called copolarized, one uses the components of the received signal that are *the same* as the transmitted-signal polarization. The second graph uses components of the received signal that are *orthogonal* to the transmitted signal.

Figure 16.46 gives a widely quoted example of this type of display for images of San Francisco.¹⁶⁶ The axes in the horizontal plane are the orientation angle for the synthesized transmitted signal ψ_t and its ellipticity angle χ_t . The vertical axis is relative power. Values of $\psi_t = 0^\circ$ and 180° are horizontal polarization, whereas $\psi_t = 90^\circ$ is vertical polarization. Linear polarization occurs when $\chi_t = 0^\circ$, and right and left circular polarizations occur when $\chi_t = \pm 45^\circ$. When the minimum is above zero, the pedestal beneath it corresponds to the unpolarized signal.

The ocean image in Figure 16.46a shows that the polarization is essentially linear, with the VV signal stronger than the HH. The cross-polarized response shows essentially no cross-polarized signal for linear transmission, but some for circularly polarized transmission.

For the park shown in Figure 16.46b, the vertically polarized linear signal is slightly higher than the horizontally polarized one. There is some cross-polarized response for the linear signal and some unpolarized signal. For the urban area shown, the strongest responses are tilted in orientation in both the copolarized and cross-polarized cases.

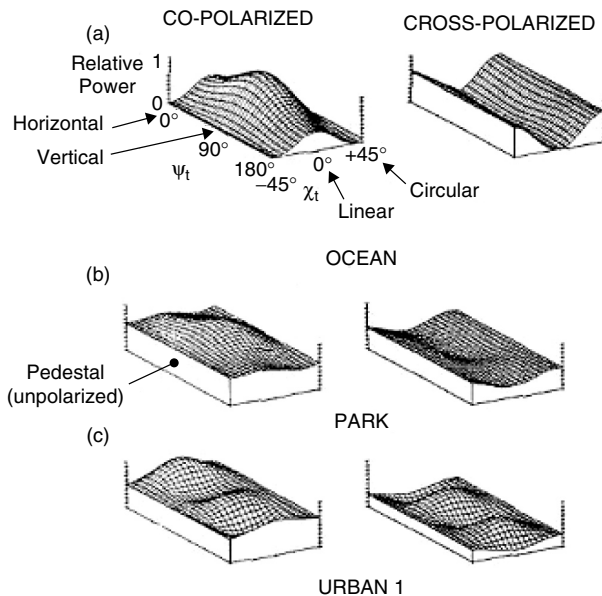


FIGURE 16.46 Selection of polarization signatures from SAR image of San Francisco: (a) an ocean area, (b) a large park, and (c) one of several urban areas (after D. L. Evans³² © IEEE 1988)

The actual numbers for the copolarized response for this case are $\chi = 0^\circ$ (VV) and $\psi = 20^\circ$.³² The reference presents similar plots showing separately the polarized and unpolarized responses.

Because of the complexity of this representation and others for polarimetric signals, one cannot as readily provide curves of response as for single-polarization images. Hence, we do not find many catalogs of polarimetric scattering responses.

Nevertheless, many authors have described the use of polarimetric images. Some of the papers using the term *polarimetric* really refer to the use of just HH, VV, and HV polarizations without regard for the phase. In this sense, they are using these images in the way that like- and cross-polarized images have been used since the start of imaging radars.¹⁶⁷ Others, however, take full advantage of the full polarization matrix.

One way to use the full matrix is to synthesize polarizations that either emphasize or suppress particular classes of targets. For example, in Figure 16.46c, one could synthesize a 20° orientation angle for a linear polarization to emphasize this class or use vertical polarization to suppress the dominant class in the image. Various authors^{168,169} have shown that one can synthesize an elliptical polarization that increases the target-to-clutter ratio where the target is, for example, a manmade object. Swartz et al.¹⁶⁹ found a polarization that gave a 9.4 dB target-to-clutter ratio where the target was an urban area and the clutter was represented by a park in the San Francisco image used to produce Figure 16.46. He found this was obtained with transmitter polarization having $(\psi_e, \chi_t) = (-41.3^\circ, -6.4^\circ)$ and receiver polarization of $(\psi_r, \chi_r) = (60.3^\circ, 3.5^\circ)$. This compares with the best result using like- and cross-polarizations without phase coherence of 7.3 dB.

Others use the three independent magnitudes of the scattering matrix and the phase angle δ between the HH and VV responses. Research has shown there is little useful information in the phase angle relating HH to cross polarization. A common use of these data is in producing state vectors to employ in discrimination of target areas, with the components of the vectors being the three magnitudes and the phase angles for each frequency used. These vectors are then used in various statistical algorithms to identify different target classes.^{170,171,172} This approach has also been used in other forests,^{173,174} agricultural areas,^{175,176} sea ice,¹⁷⁷ and snow,¹⁷⁸ and to identify surface classes of geologic significance.

An example of the use of phase difference in discriminating surface classes in the Amazon basin is illustrated in Figure 16.47.¹⁷⁹ Note the significant differences between C and X band for Macrophyte and Flooded forest. These differences could be used as discriminators to identify these classes, but normally they would simply be additional elements in the state vectors used in statistical algorithms.

16.9 SCATTERING COEFFICIENT DATA NEAR GRAZING

Conditions for backscatter near grazing incidence are sufficiently different from those at steeper incidence that they must be described separately. Here, we draw upon the work of Billingsley.¹⁷ They collected data over a wide range of terrain and unlike most previous near-grazing measurements, also collected extensive “ground-truth” information and accurately calibrated their radars. Moreover, these data were over a wide range of frequencies: VHF (167 MHz), UHF (435 MHz), L band (1.23 GHz), S band (3.24 GHz), and X band (9.2 GHz). They had 43 different target areas in different parts of the U.S. and western Canada.

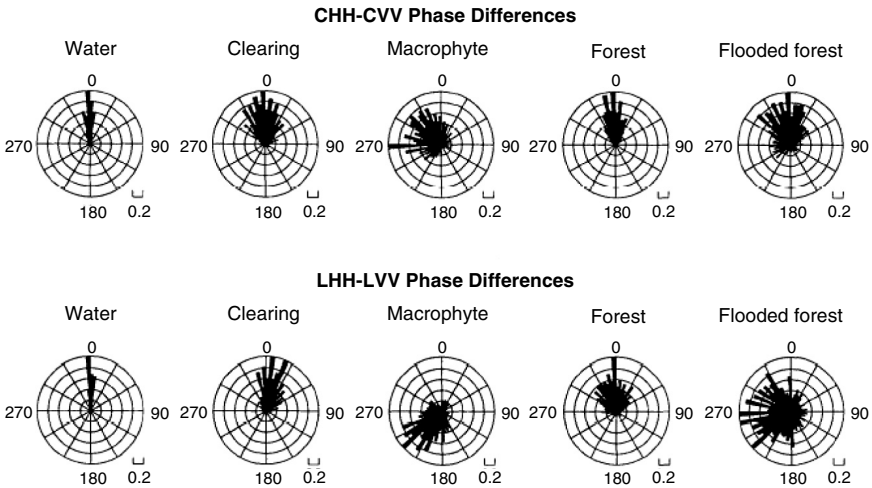


FIGURE 16.47 Phase differences for different surface classes in the Amazon basin at C band and L band¹⁷⁹

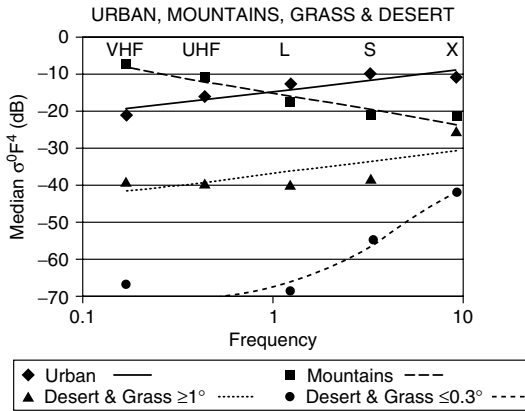
The results were described in terms of $\sigma^0 F^4$, which was called *clutter strength*. F is a propagation factor that accounts for multipath, attenuation, etc., but could not be measured separately.

Whereas *angle of incidence* is used to describe results in studies where pointing is nearer vertical, depression or grazing angle is a more appropriate description when dealing with angles where incidence is closer to horizontal. Grazing angle is the complement of incidence angle. The measurements were all at low *depression* angles, with this term used in lieu of *grazing* angle because it can be defined in terms of antenna pointing, whereas grazing angle also depends on local slope, which is both variable and, in general, unknown.

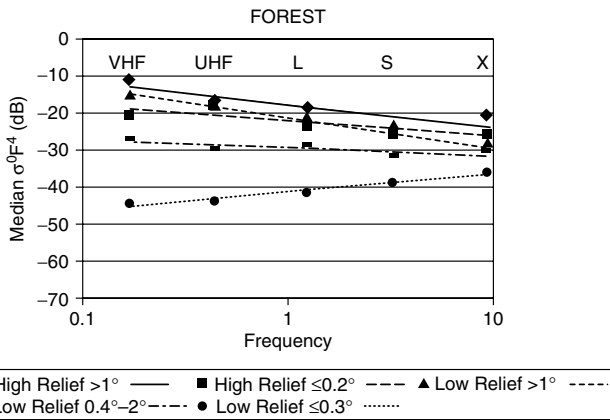
Images taken at near-grazing angles tend to be extremely “patchy” because any projections above the surface (trees, hills, buildings, fences, power lines, machinery, and vehicles) present surfaces more nearly normal to the beam. Thus nearby pixels may have clutter strength differing by tens of dB. Moreover, small slopes facing the radar increase the grazing angle, resulting in stronger echoes, whereas slopes away from the radar decrease the signal or may obliterate it by shadowing.

Because of this effect, the probability distributions of near-grazing echoes are very different from those at more moderate incidence angles. Although some small regions without significant projections or forward slopes may have Rayleigh distributions or (if only one large scatterer is present) Ricean distributions, most areas have other distributions—often Weibull or even log-normal. The result is that the mean estimated $\sigma^0 F^4$ is often much higher than the median; a few targets 10 or 20 dB higher can raise the mean a lot; even though, the targets occupy only a tiny fraction of the area. Thus, one should be careful in using mean values for radar design; the median values are more representative.

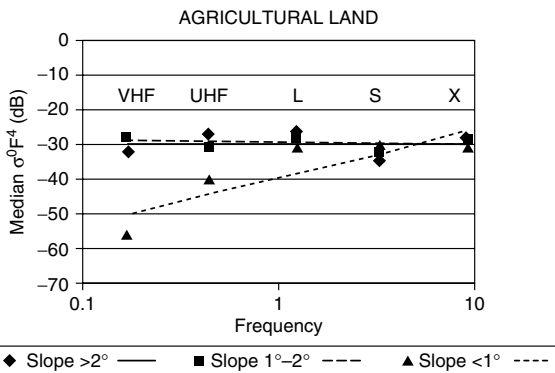
Billingsley¹⁷ presented his results both in terms of mean values and median values. Here, we report only the median values because they tend to be more meaningful for radar design than the values distorted by occasional strong targets. For most areas, little difference was found between vertical and horizontal polarizations, so the results were reported for data groups including both polarizations. Figure 16.48 shows the results, grouped by target class.



(a)



(b)



(c)

FIGURE 16.48 Median values of $\sigma^0 F^{-4}$ at low depression angles (based on Table 3.6 of Billingsley¹⁷)

For Figure 16.48*a* and *b*, the depression angle and type are the parameters, whereas for Figure 16.48*c*, the terrain slope is the parameter. The lines are based on linear regression on the logarithmic frequency scale with the exception of desert and grass at very low depression angles where a quadratic regression was used. Note that urban, mountain, and forest tend to have relatively high values compared with agriculture and uncultivated land with moderate slopes.

16.10 IMAGING RADAR INTERPRETATION

Side-looking fine-resolution imaging radars with real or synthetic apertures produce images that closely resemble aerial photographs. Both shadows and differences in σ^0 for different parts of the ground produce image-intensity variations like those in photographs. For this reason, photointerpreters can easily learn to interpret radar images. However, since the radar images are due to microwave reflectivity, not optical reflectivity, the interpreters must understand the differences and that the images at the different wavelengths are, in fact, complementary. Moreover, the geometrical distortions for radar images are those of a side-looking range measurement system, whereas those of aerial photos are those of a down-looking angle measurement system—a difference that the interpreter must understand. At low grazing angles, the distortions are small for radar, but at low incidence angles, they are large. Moreover, the speckle in radar images is not present in photographs.

Modern imaging radars use digital recording and processing, and the images are produced on film or manipulated digitally. Because the side-looking configuration produces a strip image, the output films are usually in the form of long strips. Most cameras produce separate images that are approximately square. Strip film cameras and optical-infrared scanners produce strip images like those of radars, but with different distortions because they are angle-, not range-, measuring devices.

Every pure and applied science that uses aerial photography can also use radar images. This is particularly useful in cloudy environments, but radar is also useful even in clear weather because performance is independent of time of day so sun angle does not matter. Moreover, radar ground signatures differ from those in the visible and infrared. Radar has been applied to agriculture, forestry, geology, hydrology, urban geography, regional studies, oceanography, and ice mapping.

Fading complicates the interpretation of images by producing *speckle*. This means that averaging of the speckled image usually is necessary. Sometimes the processor does the averaging, and sometimes the interpreter does it mentally; it must be done to interpret an image. The image intensity for individual pixels with a single-look SAR follows the Rayleigh distribution (actually the exponential distribution if square-law detection is used). Most SAR processors sacrifice some spatial resolution by averaging, say, four pixels together after detection. Transmitting more bandwidth than needed for range resolution accomplishes this purpose without loss of needed spatial resolution,¹⁸⁰ but it takes more transmitter power. Suitable frequency agility can accomplish the same result.

Tradeoffs exist between spatial resolution and measurement precision. The latter can be used to define a *gray-level resolution*.¹⁸¹ One can then think of image resolution in terms of a volume:

$$V = r_a r_y r_g \quad (16.33)$$

where r_a is the along-track resolution, r_y is the ground-range resolution, and r_g is the gray-level resolution. The referenced study showed that interpretability depends on V ; so tradeoffs between the three elements of V are possible. Best results for a human interpreter occur when three independent samples of the fading are averaged. Ignoring this fading (speckle) can lead to erroneous conclusions on the spatial resolution needed for a given application.

Single-frequency, single-polarization radar images are useful. However, use of multiple polarizations (particularly including cross polarization) and multiple frequencies clearly increases their value. Different angles of incidence are most suitable for different applications. For example, soil moisture monitoring is best within 20° of vertical at frequencies near 5 GHz. Vegetation discrimination is better, however, at higher frequencies and angles of incidence. For some applications, use of the full polarization matrix, including the phase, is useful. The phase information is particularly helpful in assessing scattering mechanisms, as in forests.³²

Because the literature in this field is so massive, the radar engineer wishing to learn more about the subject should consult the *Manual of Remote Sensing*,^{40,41} *Microwave Remote Sensing*,³⁷ especially Vol. III and Chapter 11 of Vol. II, and the journals outlined early in Section 16.7.

REFERENCES

1. H. Goldstein, "Sea Echo," in *Propagation of Short Radio Waves*, D. E. Kerr (ed.), MIT Radiation Laboratory Series, Chap. 6, Vol. 13, New York: McGraw-Hill Book Company, 1951.
2. R. L. Cosgriff, W. H. Peake, and R. C. Taylor, "Terrain scattering properties for sensor system design," *Terrain Handbook II*, Columbus: The Ohio State University, Eng. Exp. Sta. Antenna Lab., 1959.
3. R. K. Moore, "Radar scattering cross-section per unit area and radar astronomy," *IEEE Spectrum*, p. 156, April 1966.
4. A. K. Fung, *Microwave Scattering and Emission Models and Their Applications*. Boston: Artech House, 1994.
5. A. G. Voronovich, *Wave Scattering from Rough Surfaces*. New York: Springer-Verlag, 1994.
6. G. Ruck, D. Barrick, W. Stuart, and C. Krichbaum, *Radar Cross Section Handbook*, New York: Plenum Press, 1968.
7. R. K. Moore, "Resolution of vertical incidence radar return into random and specular components," University of New Mexico, Eng. Exp. Sta., Albuquerque, 1957.
8. J. M. Banhart (ed.) *Remote Sensing Laboratory Publication List 1964–1980*, Lawrence: University of Kansas, Remote Sensing Lab., 1981.
9. J. M. Banhart (ed.), *Remote Sensing Laboratory Publication List 1981–1983*, Vol. TR-103, Lawrence: University of Kansas, Remote Sensing Lab., 1984.
10. G. P. de Loor, P. Hoozeboom, and E. P. W. Attema, "The Dutch ROVE program," *IEEE Trans.*, vol. GE-20, pp. 3–11, 1982.
11. B. A. M. Bouman and H. W. J. vanKasteren, *Ground-based X-band Radar Backscatter Measurements of Wheat, Barley and Oats*, Wageningen Netherlands: Center for Agrobiological Research, 1989.
12. T. LeToan, "Active microwave signatures of soil and crops: significant results of three years of experiments," *Dig. Int. Geosci. Remote Sensing Symp. (IGARSS '82)*, IEEE 82CH14723-6, vol. 1, 1982.
13. Martinez, et al., "Measurements and Modeling of Vertical Backscatter Distribution in Forest Canopy," *IEEE Trans. on Geosc. and Remote Sensing*, vol. 38, pp. 710–719, 2000.
14. R. Bernard and D. Vidal-Madjar, "C-band radar cross-section of the Guyana Rain Forest: possible use as a reference target for spaceborne radars," *Remote Sensing of Envir.*, vol. 27, pp. 25–36, 1989.

15. A. R. Edison, R. K. Moore, and B. D. Warner, "Radar return measured at near-vertical incidence," *IEEE Trans. Ant. & Prop.*, vol. AP-8, pp. 246–254, 1960.
16. S. P. Gogineni and K. Jezek, "Ultra-wideband radar measurements over bare and snow-covered saline ice," *Proc. IGARSS95*, vol. 2, pp. 859–861, 1995.
17. J. B. Billingsley, *Low-Angle Radar Land Clutter: Measurements and Empirical Models*. Norwich, NY: William Andrew Publishing, 2002.
18. R. E. Clapp, "A theoretical and experimental study of radar ground return," MIT Radiat. Lab. Rept. 6024, Cambridge, MA, 1946.
19. T. S. George, "Fluctuations of ground clutter return in airborne radar equipment," *Proc. IEE (London)*, vol. 99, pp. 92–99, 1952.
20. E. A. Reitz et al., "Radar terrain return study, final report: Measurements of terrain back-scattering coefficients with an airborne X-band radar," Goodyear Aerospace Corporation, GERA-463, Phoenix, 1959.
21. J. P. Campbell, "Back-scattering characteristics of land and sea at X band," in *Proc. Natl. Conf. Aeronaut. Electron.*, 1958.
22. F. C. MacDonald, "The correlation of radar sea clutter on vertical and horizontal polarization with wave height and slope," in *IRE. Conv. Rec.*, vol. 4, 1956, pp. 29–32.
23. W. S. Ament, F. C. MacDonald, and R. Shewbridge, "Radar terrain reflections for several polarizations and frequencies," in *Proc. Symp. Radar Return, NOTS TP2359*, U.S. Naval Ordnance Test Station, Test Station, China Lake, CA, 1959.
24. C. R. Grant and B. S. Yaplee, "Backscattering from water and land at centimeter and millimeter wavelengths," *Proc. IRE.*, vol. 45, pp. 972–982, 1957.
25. Guinard et al., "Variation of the NRCS of the sea with increasing roughness," *J. Geophys. Res.*, vol. 76, pp. 1525–1538, 1971.
26. C. E. K. Livingstone, P. Singh, and A. L. Gray, "Seasonal and regional variations of active/passive microwave signatures of sea ice," *IEEE Trans.*, vol. GE-25, pp. 159–173, 1987.
27. H. McNairn et al., "Identification of agricultural tillage practices from C-band radar backscatter," *Canadian Journal of Remote Sensing*, vol. 22, 1996, pp. 154–162.
28. R. W. Larson, R. E. Hamilton, and F. L. Smith, "Calibration of synthetic aperture radar, *Dig. IGARSS '81*, pp. 938–943, 1981.
29. C. E. K. Livingstone et al., "Springtime C-band SAR backscatter signatures of Labrador Sea marginal ice: measurements versus modeling predictions," *IEEE Trans. on Geosc. and Remote Sensing*, vol. 29, pp. 29–41, 1991.
30. A. Haskell and B. M. Sorensen, "The European SAR-580 project," *Dig. IGARSS '82, IEEE 82CH14723-6*, Sess. WA-5, vol. 1.1–1.5, 1982.
31. D. N. Held, "The NASA/JPL multipolarization SAR aircraft program," *Dig. IGARSS 85*, pp. 454–457, 1985.
32. D. L. Evans et al., "Radar polarimetry: analysis tools and applications," *IEEE Trans. Geosc. & Rem. Sens.*, vol. 26, pp. 774–789, 1988.
33. Hoogeboom et al., "The PHARUS Project, Results of the Definition Study including the SAR Testbed PHARS," *IEEE Trans. on Geosc. and Remote Sensing*, vol. 30, pp. 723–735, 1992.
34. Y.-L. Desnos et al., "The ENVISAT advanced synthetic aperture radar system," *Proc. IGARSS2000*, vol. 3, pp. 1171–1173, 2000.
35. P. Fox, A. P. Luscombe, and A. A. Thompson, "RADARSAT-2 SAR modes development and utilization," *Canadian Jour. of Rem. Sens.*, vol. 30, pp. 258–264, 2004.
36. H. Wakabayashi et al., "Airborne L-band SAR system: Characteristics and initial calibration results," *Proc IGARSS'99*, vol. 1, pp. 464–466, 1999.
37. F. T. Ulaby, R. K. Moore, and A. K. Fung, *Microwave Remote Sensing: Active and Passive*, Vol. I and Vol. II, Reading, MA: Addison-Wesley Publishing Company, 1981 and 1982; Vol. III, Norwood, MA: Artech House, 1986.
38. F. T. Ulaby and M. C. Dobson, *Handbook of Radar Scattering Statistics for Terrain*, Norwood, MA: Artech House, 1989.

39. M. W. Long, *Radar Reflectivity of Land and Sea*, 2nd Ed., Norwood, MA: Artech House, 1983.
40. R. N. Colwell, D. S. Simonett, J. E. Estes, F. T. Ulaby, G. A. Thorley, et al., *Manual of Remote Sensing*, 2nd Ed., Vols. I and II, Falls Church, VA: American Society of Photogrammetry, 1983.
41. F. M. Henderson and A. J. Lewis, *Manual of Remote Sensing, Principles and Applications of Imaging Radar*, Vol. 2, 3rd Ed., New York: John Wiley & Sons, 1998.
42. J. R. Lundien, "Terrain analysis by electromagnetic means: radar responses to laboratory prepared soil samples," *U.S. Army Waterways Exp. Sta., TR 3-639*, Vicksburg, MS, 1966.
43. L. K. Wu, R. K. Moore, R. Zoughi, F. T. Ulaby, and A. Afifi, "Preliminary results on the determination of the sources of scattering from vegetation canopies at 10 GHz," pts. I and II, *Int. J. Remote Sensing*, vol. 6, pp. 299–313, 1985.
44. L. K. Wu, R. K. Moore, and R. Zoughi, "Sources of scattering from vegetation canopies at 10 GHz," *IEEE Trans.*, vol. GE-23, pp. 737–745, 1985.
45. R. Zoughi, J. Bredow, and R. K. Moore, "Evaluation and comparison of dominant backscattering sources at 10 GHz in two treatments of tall-grass prairie," *Remote Sensing Environ.*, vol. 22, pp. 395–412, 1987.
46. R. Zoughi, L. K. Wu, and R. K. Moore, "Identification of major backscattering sources in trees and shrubs at 10 GHz," *Remote Sensing Environ.*, vol. 19, pp. 269–290, 1986.
47. J. F. Paris, "Probing thick vegetation canopies with a field microwave spectrometer," *IEEE Trans.*, vol. GE-24, pp. 886–893, 1986.
48. S. T. Wu, "Preliminary report on measurements of forest canopies with C-Band radar scatterometer at NASA/NSTL," *IEEE Trans.*, vol. GE-24, November 1986.
49. D. E. Pitts, G. D. Badhwar, and E. Reyna, "The Use of a helicopter mounted ranging scatterometer for estimation of extinction and scattering properties of forest canopies," *IEEE Trans.*, vol. GE-26, pp. 144–152, 1988.
50. R. Bernard, M. E. Frezal, D. Vidal-Madjar, D. Guyon, and J. Riom, "Nadir looking airborne radar and possible applications to forestry," *Remote Sensing Environ.*, vol. 21, pp. 297–310, 1987.
51. S. L. Durden, J. D. Klein, and H. A. Zebker, "Polarimetric radar measurements of a forested area near Mt. Shasta," *IEEE Trans. on Geosc. and Remote Sensing*, vol. 29, pp. 444–450, 1991.
52. D. K. Barton, "Land clutter models for radar design and analysis," *Proc. IEEE*, vol. 73, pp. 198–204, 1985.
53. R. K. Moore, *Traveling Wave Engineering*, New York: McGraw-Hill Book Company, 1960.
54. A. H. Schooley, "Upwind-downwind ratio of radar return calculated from facet size statistics of wind disturbed water surface," *Proc. IRE*, vol. 50, pp. 456–461, 1962.
55. D. O. Muhleman, "Radar scattering from venus and the moon," *Astron. J.*, vol. 69, pp. 34–41, 1964.
56. A. K. Fung, "Theory of cross polarized power returned from a random surface," *Appl. Sci. Res.*, vol. 18, pp. 50–60, 1967.
57. I. Katz and L. M. Spetner, "Two statistical models for radar return," *IRE Trans.*, vol. AP-8, pp. 242–246, 1960.
58. P. Beckmann and A. Spizzichino, *The Scattering of Electromagnetic Waves from Rough Surfaces*, New York: Macmillan Company, 1963.
59. P. Beckmann, "Scattering by composite rough surfaces," *Proc. IEEE*, vol. 53, pp. 1012–1015, 1965.
60. A. K. Fung and H. J. Eom, "An approximate model for backscattering and emission from land and sea," *Dig. IGARSS '81*, vol. I, pp. 620–628, 1981.
61. H. S. Hayre and R. K. Moore, "Theoretical scattering coefficients for near-vertical incidence from contour maps," *J. Res. Nat. Bur. Stand.*, vol. 65D, pp. 427–432, 1961.
62. H. Davies, "The reflection of electromagnetic waves from a rough surface," *Proc. IEE (London)*, pt. 4, vol. 101, pp. 209–214, 1954.
63. A. K. Fung and R. K. Moore, "The correlation function in Kirchoff's method of solution of scattering of waves from statistically rough surfaces," *J. Geophys. Res.*, vol. 71, pp. 2929–2943, 1966.

64. J. V. Evans and G. H. Pettengill, "The scattering behavior of the moon at wavelengths of 3.6, 68, and 784 centimeters," *J. Geophys. Res.*, vol. 68, pp. 423–447, 1963.
65. J. W. Wright, "A new model for sea clutter," *IEEE Trans.*, vol. AP-16, pp. 217–223, 1968.
66. F. G. Bass, I. M. Fuks, A. I. Kalmykov, I. E. Ostrovsky, and A. D. Rosenberg, "Very high frequency radiowave scattering by a disturbed sea surface," *IEEE Trans.*, vol. AP-16, pp. 554–568, 1968.
67. S. O. Rice, "Reflection of electromagnetic waves by slightly rough surfaces," *Commun. Pure Appl. Math.*, vol. 4, pp. 351–378, 1951.
68. Ref. 37, vol. II, p. 961.
69. Ref. 37, vol. II, chap. 12.
70. Ref. 37, vol. III, chap. 13.
71. R. H. Lang and J. S. Sidhu, "Electromagnetic scattering from a layer of vegetation: a discrete approach," *IEEE Trans.*, vol. GE-21, pp. 62–71, 1983.
72. A. K. Fung, "A review of volume scatter theories for modeling applications," *Radio Sci.*, vol. 17, pp. 1007–1017, 1982.
73. Y. S. Kim, "Theoretical and experimental study of radar backscatter from sea ice," Ph.D. dissertation, University of Kansas, Lawrence, 1984.
74. J. M. Stiles and K. Sarabandi, "Electromagnetic scattering from grassland—Part I: A fully phase-coherent scattering model," *IEEE Transactions on Geoscience and Remote Sensing*, vol. 38, pp. 339–348, 2000.
75. H. O. Rydstrom, "Interpreting local geology from radar imagery," *Bull. Geol. Soc. Am.*, vol. 78, pp. 429–436, 1967.
76. W. K. Lee, "Analytical investigation of urban SAR features having a group of corner reflectors," *IGARSS 2001*, vol. 3, pp. 1262–1264, 2001.
77. M. F. Chen and A. K. Fung, "A study of the validity of the integral equation model by moment method simulation—cylindrical case," *Remote Sensing of Envir.*, vol. 29, pp. 217–228, 1989.
78. A. K. Fung, M. R. Shah, and S. Tjuatja, "Numerical simulation of scattering from three-dimensional randomly rough surfaces," *IEEE Trans. on Geosc. and Remote Sensing*, vol. 32, pp. 986–994, 1994.
79. S. O. Rice, "Mathematical analysis of random noise," pt. 1, *Bell Syst. Tech. J.*, vol. 23, pp. 282–332, 1944; pt. II, vol. 24, pp. 46–156, 1945.
80. G. A. Shmidman, "Generalized radar clutter model," *IEEE Trans. on Aerosp. Elec. Sys.*, vol. 35, pp. 857–865, 1999.
81. R. D. DeRoo et al., "MMW scattering characteristics of terrain at near-grazing incidence," *IEEE Trans. on Aerosp. Elec. Sys.*, vol. 35, pp. 1010–1018, 1999.
82. J. B. Billingsley et al., "Statistical analyses of measured radar ground clutter data," *IEEE Trans. Aerosp. & Electron. Sys.* vol. 35, pp. 579–593, 1999.
83. Ref. 37, vol. II, pp. 487–492.
84. F. T. Ulaby, W. H. Stiles, D. Brunfeldt, and E. Wilson, "1–35 GHz microwave scatterometer," in *Proc. IEEE/MTT-S, Int. Microwave Symp.*, IEEE 79CH1439-9 MIT-S, 1979.
85. D. R. Brunfeldt and F. T. Ulaby, "An active radar calibration target," *Dig. IGARSS '82, IEEE 82CH14723-6*, 1982.
86. A. Freeman, Y. Shen, and C. L. Werner, "Polarimetric SAR calibration experiment using active radar calibrators," *IEEE Trans. on Geosc. and Remote Sensing*, vol. 28, pp. 224–240, 1990.
87. Ref. 37, vol. II, pp. 766–779.
88. F. J. Janza, "The analysis of a pulse radar acquisition system and a comparison of analytical models for describing land and water radar return phenomena," Ph.D. dissertation, University of New Mexico, Albuquerque, 1963.
89. F. J. Janza, R. K. Moore, and R. E. West, "Accurate radar attenuation measurements achieved by inflight calibration," *IEEE Trans.*, vol. PGI-4, pp. 23–30, 1955.
90. E. M. Bracalente, W. L. Jones, and J. W. Johnson, "The Seasat—a satellite scatterometer," *IEEE Trans.*, vol. OE-2, pp. 200–206, 1977.

91. F. K. Li, D. Callahan, D. Lame, and C. Winn, "NASA scatterometer on NROSS—a system for global observations on ocean winds," *Dig. IGARSS '84*, 1984.
92. R. K. Moore and W. J. Pierson, "Measuring sea state and estimating surface winds from a polar orbiting satellite," in *Proc. Int. Symp. Electromagn. Sensing of Earth from Satellites*, 1965, pp. R1–R26.
93. L. J. Cote et al., "The directional spectrum of a wind-generated sea as determined from data obtained by the stereo wave observation project," *New York University Meteorol. Pap.*, vol. 2, no. 66, 1960.
94. S. P. Gogineni et al., "Application of plane waves for accurate measurement of microwave scattering from geophysical surfaces," *IEEE Transactions on Geoscience and Remote Sensing*, vol. 33, pp. 627–633, 1995.
95. T. F. Bush and F. T. Ulaby, "4–18 GHz radar spectrometer," University of Kansas, Remote Sensing Lab., vol. TR 177-43, Lawrence, September 1973.
96. Ref. 37, vol. II, pp. 779–791; vol. III, chap. 14.
97. R. Zoughi, L. K. Wu, and R. K. Moore, "SOURCESCAT: A very fine resolution radar scatterometer," *Microwave J.*, vol. 28, pp. 183–196, 1985.
98. S. P. Gogineni, F. A. Hoover, and J. W. Bredow, "High-performance, inexpensive polarimetric radar for in situ measurements," *Proc. IGARSS89*, vol. 28, pp. 450–455, 1990.
99. R. K. Moore, "Effect of pointing errors and range on performance of dual-pencil-beam scatterometers," *IEEE Trans.*, vol. GE-23, pp. 901–905, 1985.
100. A. R. Edison, "An acoustic simulator for modeling backscatter of electromagnetic waves," Ph.D. dissertation, University of New Mexico, Albuquerque, 1961.
101. B. E. Parkins and R. K. Moore, "Omnidirectional scattering of acoustic waves from rough surfaces of known statistics," *J. Acoust. Soc. Am.*, vol. 50, pp. 170–175, 1966.
102. R. K. Moore, "Acoustic Simulation of radar returns," *Microwaves*, vol. 1, no. 7, pp. 20–25, 1962.
103. M. C. Dobson, F. T. Ulaby, D. R. Brunfeldt, and D. N. Held, "External calibration of SIR-B imagery with area-extended and point targets," *IEEE Trans.*, vol. GE-24, pp. 453–461, 1986.
104. D. Vaillant and A. Wadsworth, "Preliminary results of some remote sensing campaigns of the French Airborne SAR VARAN-S," *Dig. IGARSS '86*, pp. 495–500, 1986.
105. H. Hirose and Y. Matsuzaka, "Calibration of cross-polarized SAR imagery using dihedral corner reflectors," *Dig. IGARSS '86*, pp. 487–492, 1986.
106. D. R. Brunfeldt and F. T. Ulaby, "Active reflector for radar calibration," *IEEE Trans.*, vol. GE-22, pp. 165–169, 1984.
107. P. Hartl, M. Reich, and S. Bhagavathula, "An attempt to calibrate air-borne SAR image using active radar calibrators and ground-based scatterometers," *Dig. IGARSS 86*, pp. 501–508, 1986.
108. R. W. Larson et al., "Bistatic clutter measurements," *IEEE Trans.*, vol. AP-26, pp. 801–804, 1978.
109. J. Renau and J. A. Collinson, "Measurements of electromagnetic backscattering from known rough surfaces," *Bell Syst. Tech. J.*, vol. 44, pp. 2203–2226, 1965.
110. D. Kieu, "Effect of tall structures on microwave communication systems," M.S. thesis, University of Kansas, Lawrence, 1988.
111. F. T. Ulaby et al., "Millimeter-wave bistatic scattering from ground and vegetation targets," *IEEE Trans. Geosc. & Rem. Sens.*, vol. GE-26, pp. 229–243, 1988.
112. T.-K. Chan et al., "Experimental studies of bistatic scattering from two-dimensional conducting random rough surfaces," *IEEE Trans. on Geosc. and Remote Sensing*, vol. 34, pp. 674–680, 1996.
113. W. H. Stiles, D. Brunfeldt, and F. T. Ulaby, "Performance analysis of the MAS (Microwave Active Spectrometer) systems: calibration, precision and accuracy," University of Kansas, Remote Sensing Lab., vol. TR 360-4, Lawrence, 1979.
114. F. T. Ulaby et al., "1-35 GHz microwave scatterometer," *Proc. IEEE/MTT-S 1979 Intl. Microwave Symp.*, vol. '79CH1439-9 MTT-S', 1979.

115. R. K. Moore, K. A. Soofi, and S. M. Purduski, "A radar clutter model: average scattering coefficients of land, snow, and ice," *IEEE Trans.*, vol. AES-16, pp. 783–799, 1980.
116. R. K. Moore et al., "Simultaneous active and passive microwave response of the Earth—the Skylab RADSCAT experiment," in *Proc. Ninth Int. Symp. Remote Sensing Environ.*, University of Michigan, Ann Arbor, 1974, pp. 189–217.
117. Ref. 21. See summaries in vol. II, chap. 11, and vol. III, chap. 21.
118. F. T. Ulaby, "Vegetation clutter model," *IEEE Trans.*, vol. AP-28, pp. 538–545, 1980.
119. W. H. Stiles and F. T. Ulaby, "The active and passive microwave response to snow parameters, part I: wetness," *J. Geophys. Res.*, vol. 85, pp. 1037–1044, 1980.
120. F. T. Ulaby and W. H. Stiles, "The active and passive microwave response to snow parameters, part II: water equivalent of dry snow," *J. Geophys. Res.*, vol. 85, pp. 1045–1049, 1980.
121. I. J. Birrer, E. M. Bracalante, G. J. Dome, J. Sweet, and G. Berthold, "Signature of the Amazon rain forest obtained with the Seasat scatterometer," *IEEE Trans.*, vol. GE-20, pp. 11–17, 1982.
122. R. Bernard and D. Vidal-Madjar, "C-band radar cross-section of the Guyana rain forest: possible use as a reference target for spaceborne radars," *Remote Sensing of Envir.*, vol. 27, pp. 25–36, 1989.
123. R. K. Moore and M. Hemmat, "Determination of the vertical pattern of the SIR-B antenna," *Int'l Jour. Rem. Sens.*, vol. 9, pp. 839–847, 1988.
124. M. Shimada, "Long-term stability of L-band normalized radar cross section of Amazon rainforest using the JERS-1 SAR," *Canadian Jour. of Rem. Sens.*, vol. 31, pp. 132–137, 2005.
125. A. R. Edison, R. K. Moore, and B. D. Warner, "Radar return measured at near-vertical incidence," *IEEE Trans.*, vol. AP-8, pp. 246–254, 1960.
126. C. H. Bidwell, D. M. Gragg, and C. S. Williams: "Radar return from the vertical for ground and water surface," Sandia Corporation, Albuquerque, NM, 1960.
127. Y. S. Kim, R. K. Moore, R. G. Onstott, and S. P. Gogineni, "Towards identification of optimum radar parameters for sea-ice monitoring," *J. Glaciol.*, vol. 31, pp. 214–219, 1985.
128. T. LeToan et al., "Multitemporal and dual-polarization observations of agricultural vegetation covers by X-band SAR images," *IEEE Trans. on Geosc. and Remote Sensing*, vol. GE-27, pp. 709–718, 1989.
129. B. A. M. Bouman and H. W. J. vanKasteren, *Ground-based X-band Radar Backscatter Measurements of Wheat, Barley and Oats*, Wageningen NETHERLANDS: Center for Agrobiological Research, 1989.
130. B. Brisco, R. J. Brown, and G. J. Sofko, "The CCRS ground-based microwave facility," *IGARSS88*, vol. 1, pp. 575–576, 1988.
131. E. Stotzer, V. Wegmuller, R. Huppi, and C. Matzler, "Dielectric and surface parameters related to microwave scatter and emission properties," *Dig. IGARSS '86*, pp. 599–609, 1986.
132. T. Nagler and H. Rott, "Retrieval of wet snow by means of multitemporal SAR data," *IEEE Trans. on Geosc. and Remote Sensing*, vol. 38, pp. 754–765, 2000.
133. F. J. Janza, R. K. Moore, and B. D. Warner, "Radar cross-sections of terrain near vertical incidence at 415 Mc, 3800 Mc, and extension of analysis to X band," University of New Mexico, Eng. Exp. Sta., TR EE-21, Albuquerque, 1959.
134. Ref. 37, vol. III, Fig. 21.20, p. 1825.
135. Ref. 37, vol. III, Fig. 21.22, p. 1827.
136. Ref. 37, vol. III, Fig. 21.41, p. 1856.
137. D. H. Hoekman, "Radar backscattering of forest stands," *Int. J. Remote Sensing*, vol. 6, pp. 325–343, 1985.
138. D. H. Hoekman et al., "Land cover type and biomass classification using AirSAR data for evaluation of monitoring scenarios in the Columbian Amazon," *IEEE Trans. on Geosc. and Remote Sensing*, vol. 38, pp. 685–696, 2000.
139. M. C. Dobson and F. T. Ulaby, "Microwave backscatter dependence on surface roughness, soil moisture and soil texture: Part III—soil tension," *IEEE Trans.*, vol. GE-19, pp. 51–61, 1981.

140. T. J. Schmugge, "Effect of texture on microwave emission from soils," *IEEE Trans.*, vol. GE-18, pp. 353–361, 1980.
141. F. T. Ulaby, A. Aslam, and M. C. Dobson, "Effects of vegetation cover on the radar sensitivity to soil moisture," University of Kansas, Remote Sensing Lab., TR 460-10, Lawrence, 1981.
142. M. C. Dobson, F. Kouyate, and F. T. Ulaby, "A reexamination of soil textural effects on microwave emission and backscattering," *IEEE Trans.*, vol. GE-22, pp. 530–535, 1984.
143. F. T. Ulaby, B. Brisco, and M. C. Dobson, "Improved spatial mapping of rainfall events with spaceborne SAR imagery," *IEEE Trans.*, vol. GE-21, pp. 118–121, 1983.
144. F. T. Ulaby, M. C. Dobson, J. Stiles, R. K. Moore, and J. C. Holtzman, "A simulation study of soil moisture estimation by a space SAR," *Photogramm. Eng. Remote Sensing*, vol. 48, pp. 645–660, 1982.
145. Z. Li et al., "Soil moisture measurement and retrieval using envisat asar imagery," *Proc. IGARSS04*, vol. V, pp. 3539–3542, 2004.
146. J. Shi et al., "Estimation of soil moisture with L-band multipolarization radar," *Proc. IGARSS04*, vol. II, pp. 815–818, 2004.
147. Y. Kim and J. van Zyl, "Vegetation effects on soil moisture estimation," *Proc. IGARSS04*, vol. II, pp. 800–802, 2004.
148. E. Attema and F. T. Ulaby, "Vegetation modeled as a water cloud," *Radio Sci.*, vol. 13, pp. 357–364, 1978.
149. Ref. 37, vol. III, p. 1873.
150. H. Eom and A. K. Fung, "A scatter model for vegetation up to K_u -band," *Remote Sensing Environ.*, vol. 15, pp. 185–200, 1984.
151. W. H. Stiles and F. T. Ulaby "The active and passive microwave response to snow parameters, Part I: Wetness," *J. Geophys. Res.*, vol. 85, pp. 1037–1044, 1980.
152. W. H. Stiles, F. T. Ulaby, A. K. Fung, and A. Aslam, "Radar spectral observations of snow," *Dig. IGARSS '81*, pp. 654–668, 1981.
153. A. V. Bushuyev, N. A. Volkov, and V. S. Loshchilov, *Atlas of Ice Formations*, Leningrad: Gidrometeoizdat, 1974. (In Russian with English annotations.)
154. A. L. Gray, R. K. Hawkins, C. E. Livingstone, L. D. Arsenaault, and W. M. Johnstone, "Simultaneous scatterometer and radiometer measurements of sea ice microwave signatures," *IEEE J.*, vol. OE-7, pp. 20–32, 1982.
155. V. S. Loshchilov and V. A. Voyevodin, "Determining elements of drift of the ice cover and movement of the ice edge by the aid of the 'Toros' side scanning radar station," *Probl. Arktiki Antarkt* (in Russian), vol. 40, pp. 23–30, 1972.
156. S. Haykin et al., *Remote Sensing of Sea Ice and Icebergs*, New York: Wiley-IEEE, 1994.
157. R. K. Raney et al., "RADARSAT," *Proc. IEEE*, vol. 79, pp. 839–849, 1991.
158. B. Ramsay et al., "Use of RADARSAT data in the Canadian ice service," *Canadian Journal of Remote Sensing*, vol. 24, pp. 36–42, 1998.
159. G. I. Belchansky and D. C. Douglas, "Seasonal comparisons of sea ice concentration estimates derived from SSM/I, OKEAN, and RADARSAT data," *Rem. Sens. Envir.*, vol. 81, pp. 67–81, 2002.
160. M. Nazirov, A. P. Pichugin, and Y. G. Spiridonov, *Radiolokatsia Poverchnosti Zemli Iz-Kosmosa (Radar Observation of the Earth from Space)*, Leningrad: Hydrometeoizdat, 1990. (In Russian.)
161. Mitnik et al., "Structure and dynamics of the Sea of Okhotsk marginal ice zone from 'ocean' satellite radar sensing data," *J. Geophys. Res.*, vol. 97, pp. 7249–7445, 1992.
162. M. R. Drinkwater, R. Hosseimostafa, and S. P. Gogineni, "C-band backscatter measurements of winter sea-ice in the Weddell Sea, Antarctica," *International Journal of Remote Sensing*, vol. 16, pp. 3365, 1995.
163. F. T. Ulaby and C. Elachi, *Radar Polarimetry for Geoscience Applications*. Boston: Artech House, 1990.

164. M. A. Sletten and D. J. McLaughlin, "Radar polarimetry," in *Wiley Encyclopedia of Electrical and Electronics Engineering Online*, J. Webster (ed.), New York: John Wiley & Sons, Inc., 1999.
165. J. van Zyl and Y. Kim, "Remote sensing by radar," in *Wiley Encyclopedia of Electrical and Electronics Engineering Online*, J. Webster (ed.), New York: John Wiley & Sons, Inc., 1999.
166. W. M. Boerner et al., "On the basic principles of radar polarimetry: the target characteristic polarization state theory of Kennaugh, Huynen's polarization fork concept, and its extension to the partially polarized case," *Proc. IEEE*, vol. 79, pp. 1538–1550, 1990.
167. J. J. van Zyl, H. Zebker, and D. N. Held, "Imaging radar polarization signatures: Theory and observation," *Radio Sci.*, vol. 22, pp. 529–543, 1987.
168. S. A. Morain and D. S. Simonett, "K-band radar in vegetation mapping," *Photog. Eng. and Rem. Sens.*, vol. 33, pp. 730–740, 1967.
169. P. C. Dubois and J. van Zyl, "Polarization filtering of SAR data," *Digest IGARSS88*, vol. 3, pp. 1816–1819, 1989.
170. A. A. Swartz et al., "Optimal polarization for achieving maximum contrast in radar images," *J. Geophys. Res.*, vol. 93, pp. 15252–15260, 1988.
171. S. R. Cloude and E. Pottier, "An entropy based classification scheme for land applications of polarimetric SAR," *IEEE Trans. on Geosc. and Remote Sensing*, vol. 35, pp. 68–78, 1997.
172. J. van Zyl, "Unsupervised classification of scattering behavior using radar polarimetry data," *IEEE Trans. Geosc. Rem. Sens.*, vol. 27, pp. 36–45, 1989.
173. Touzi et al., "Polarimetric discriminators for SAR images," *IEEE Trans. on Geosc. and Remote Sensing*, vol. 30, pp. 973–980, 1992.
174. S. L. Durden, J. D. Klein, and H. A. Zebker, "Polarimetric radar measurements of a forested area near Mt. Shasta," *IEEE Trans. on Geosc. and Remote Sensing*, vol. 29, pp. 111–450, 1991.
175. Hoekman et al., "Biophysical forest type characterization in the Columbian Amazon by airborne polarimetric SAR," *IEEE Trans. on Geosc. and Remote Sensing*, vol. 40, pp. 1288–1300, 2002.
176. P. Ferrazzoli et al., "The potential of multifrequency polarimetric SAR in assessing agricultural and arboreous biomass," *IEEE Trans. on Geosc. and Remote Sensing*, vol. 35, pp. 5–17, 1997.
177. Inoue et al., "Season-long daily measurements of multifrequency (Ka, Ku, X, C, and L) and full-polarization backscatter signatures over paddy rice field and their relationship with biological variables," *Remote Sensing of Envir.*, vol. 81, pp. 194–204, 2002.
178. S. V. Nghiem et al., "Polarimetric signatures of sea ice, 2, experimental observations," *J. Geophys. Res.*, vol. 100, pp. 13681–13698, 1995.
179. A. Martini, L. Ferro-Famil, and E. Pottier, "Multi-frequency polarimetric snow discrimination in alpine areas," *Proc. IGARSS04*, vol. VI, pp. 3684–3687, 2004.
180. L. L. Hess et al., "Delineation of inundated area and vegetation along the Amazon floodplain with the SIR-C synthetic aperture radar," *IEEE Trans. on Geosc. and Remote Sensing*, vol. 33, pp. 896–904, 1995.
181. R. K. Moore, W. P. Waite, and J. W. Rouse, "Panchromatic and polypanchromatic radar," *Proc. IEEE*, vol. 57, pp. 590–593, 1969.
182. R. K. Moore, "Tradeoff between picture element dimensions and noncoherent averaging in side-looking airborne radar," *IEEE Trans.*, vol. AES-15, pp. 696–708, 1979.

